NOVA SCHOOL OF SCIENCE & TECHNOLOGY

DEPARTMENT OF PHYSICS

PEDRO MIGUEL ALVES GUERREIRO

BSc in Physics Engineering

LOW TOTAL ELECTRON YIELD N-DOPED GRAPHENE COATINGS PRODUCED BY ELECTROPHORETIC DEPOSITION

MASTER IN PHYSICS ENGINEERING

NOVA University Lisbon
September, 2025

NOVA SCHOOL OF SCIENCE & TECHNOLOGY

DEPARTMENT OF PHYSICS

LOW TOTAL ELECTRON YIELD N-DOPED GRAPHENE COATINGS PRODUCED BY ELECTROPHORETIC DEPOSITION

PEDRO MIGUEL ALVES GUERREIRO

BSc in Physics Engineering

Adviser: Nenad Bundaleski
Auxiliar Professor, NOVA FCT

Examination Committee

Chair: Yuri Fonseca da Silva Nunes
Auxiliar Professor, FCT-NOVA

Rapporteur: Susana Isabel dos Santos Silva Sério Venceslau
Auxiliar Professor, FCT-NOVA

Member: Nenad Bundaleski
Auxiliar Professor, FCT-NOVA

MASTER IN PHYSICS ENGINEERING

NOVA University Lisbon
September, 2025

LOW TOTAL ELECTRON YIELD N-DOPED GRAPHENE COATINGS PRODUCED BY ELECTROPHORETIC DEPOSITION

This document was created with the (pdf/Xe/Lua)LaTeX processor and the NOVAthesis template (v7.3.9) [1].

Acknowledgements

É com um enorme prazer que agradeço ao meu orientador Nenad Bundaleski por me ter ajudado ao longo desta jornada académica. Graças a si, pude reviver o gosto pela física que sempre esteve em mim. Também agradeço por todos os momentos e ensinamentos que me deu e que com eles seguirei para o resto da minha vida e carreira.

Também gostaria de agradecer ao professor Orlando Teodoro por me ter introduzido ao grupo CEFITEC/METROVAC e por me ter prestado todo o apoio, sempre que precisei. Também um grande obrigado ao Orlando Junior, à Carolina e à Dr. Ana Fonseca por me terem acompanhado e ajudado durante todo o tempo que estive no laboratório. Muito obrigado ao Sr. Afonso e ao Sr. Bruno por todo o suporte durante a minha tese e o meu percurso académico.

Não posso deixar de agradecer à doutora Neli Bundaleska e ao resto da equipa od Laboratório de Plasma Engineering do IPFN, IST, por me terem fornecido o material necessário para a concretização deste trabalho, sendo este tanto o grafeno como o grafeno dopado com azoto, assim como por terem feito Cristolografia de Raios-X do grafeno dopado e Espetroscopia de Raman do grafeno.

Deixo aqui um obrigado e os parabéns aos meus colegas de curso, sem vocês este curso não seria o mesmo. Mas tenho que agradecer especialmente ao Tomás, um rapaz muito bondoso e inteligente que sempre esteve disposto a ajudar-me quando precisei, e ao Francisco, um rapaz mais chill, mas sempre de olho em mim, com os braços abertos para o quer que fosse que me fizesse bem, que estão comigo desde o primeiro ano de faculdade e que fizeram cada dia da semana, seja dentro ou fora da faculdade, memorável. Também não poderia deixar um grande obrigado ao meu grande companheiro de trabalho Gonçalo Marujo, que, apesar de ser brincalhão e gostar de sistemas governamentais duvidosos, foi ele que uniu o curso como uma família. A personificação da palavra amigo. Também gostaria de agradecer à Leonor, à Ana Neves, à Mariana e ao Jorge. Sem vocês o curso e a minha vida teriam sido mais monótonos. Pode não parecer, mas vocês traziam mais vida e cor ao grupo.

À minha família, um grandíssimo obrigado por todo apoio e amor que me deram durante estes 5 anos de faculdade. Quero que saibam que vos respeito e vos respeitarei

para o resto da minha vida com muito amor.

Não podia esquecer de agradecer ao Miguel, meu irmão de alma, que sempre me acompanhou a minha vida inteira e que não foi diferente durante estes 5 anos. E também à Polly, uma grande amiga na qual sempre pude confiar tudo. Também gostaria de agradecer à Carlota, à Mara e à Beatriz, cuja amizade cresceu muito durante estes 5 anos apesar de as ter conhecido fora da faculdade.

Não poderia deixar de desejar um obrigado mais que especial à minha parceira de vida e de laboratório, aka my love. Tu tornaste estes 8 meses de tese em algo inimaginável. Tu foste a minha inspiração para a escrita, tu foste a minha criatividade para a análise de resultados e o meu ombro direito para os dias em que me senti mais em baixo. Sem ti, este semestre não teria sido nem metade do que foi. Muito obrigado do fundo do coração.

Abstract

Low secondary electron emission (SEE) materials have gained significant attention in recent years, particularly in aerospace technologies, such as RF devices for satellite communications, and in fundamental particle physics studies. In high-intensity particle accelerators such as the High Luminosity Large Hadron Collider (HL-LHC) at CERN, materials with low SEE are crucial for mitigating electron cloud formation, thereby enabling higher maximum beam intensities, improved thermal conditions, and more reliable experimental results. This phenomenon results from the multipacting effect: electrons are generated either through ionization of the residual gas or via the photoelectric effect induced by synchrotron radiation. These high-energy electrons subsequently collide with the accelerator walls, producing secondary electrons. The electric field, produced by the bunches of positive particles, accelerates these secondary electrons, triggering a localized avalanche. The most common strategy to reduce the electron cloud formation is to coat the inner walls of accelerators with low Total Electron Yield (TEY) materials. Graphene is a promising candidate due to its inherently low SEE and surface roughness, which further reduces TEY. Recent studies revealed that nitrogen doping into graphene can lower its Secondary Electron Yield (SEY) even further, while also mitigating aging effects caused by repeated exposure to air. In this project, N-doped graphene free-standing powder was deposited onto metallic substrates, similar to those used as accelerator inner walls, using electrophoretic deposition (EPD). This technique was chosen for its ability to preserve the material's original properties while offering a simple and cost-effective deposition method. Following the sample preparation, X-ray Photoelectron Spectroscopy (XPS) was used to characterize the samples in terms of surface chemical composition, while TEY measurements were performed. This allowed the identification of optimal deposition parameters and enabled the establishment of correlations between material characteristics and the TEY performance.

Keywords: Secondary Electron Emission · Total Electron Yield · Particle Accelerators · Electron Cloud · Graphene · Nitrogen Doping · Electrophoretic Deposition · X-ray Photoelectron Spectroscopy

Resumo

Materiais com baixa Emissão de Eletrões Secundários (SEE) têm ganho uma atenção significativa nos últimos anos, particularmente em tecnologias aeroespaciais, como dispositivos de RF para comunicações por satélite, e em estudos fundamentais de física de partículas. Em aceleradores de partículas de alta intensidade, como o *High Luminosity Large Hadron Collider* (HL-LHC) do CERN, materiais com baixa SEE são cruciais para mitigar a formação de nuvens de eletrões, permitindo assim maiores intensidades máximas de feixe, melhores condições térmicas e resultados experimentais mais fiáveis. Este fenómeno resulta do efeito de *multipacting*: os eletrões são gerados quer através da ionização do gás residual, quer pelo efeito fotoelétrico induzido pela radiação sincrotrão. Estes eletrões de alta energia colidem subsequentemente com as paredes do acelerador, produzindo eletrões secundários. O campo elétrico, gerado pelos feixes de partículas positivas, acelera estes eletrões secundários, desencadeando uma avalanche localizada. A estratégia mais comum para reduzir a formação de nuvens de eletrões consiste em revestir as paredes internas dos aceleradores com materiais de baixo *Total Electron Yield* (TEY). O grafeno surge como um candidato promissor devido à sua baixa SEE e à sua rugosidade superficial, que contribui para uma redução adicional do TEY. Estudos recentes revelaram que a dopagem do grafeno com azoto pode reduzir ainda mais a sua *Secondary Electron Yield* (SEY), ao mesmo tempo que mitiga os efeitos de envelhecimento causados por exposições repetidas ao ar. Neste projeto, pó de grafeno dopado com azoto, foi depositado sobre substratos metálicos semelhantes aos utilizados nas paredes internas dos aceleradores, através do método de deposição eletroforética (EPD). Esta técnica foi escolhida pela sua capacidade de preservar as propriedades originais do material, oferecendo simultaneamente um método de deposição simples e económico. Após a preparação das amostras, foi utilizada Espetroscopia de Fotoeletrões por Raios-X (XPS) para caracterizar a composição química superficial, e medido o TEY. Estes procedimentos permitiram identificar os parâmetros de deposição ótimos e estabelecer correlações entre as características do material e o seu TEY.

Palavras-chave: Emissão de Eletrões Secundários · Total Electron Yield · Aceleradores de

partículas · Nuvem de Eletrões · Grafeno · Dopagem com Azoto · Deposição Eletroforética · Espetroscopia de Fotoeletrões por Raios-X

Contents

List of Figures

List of Tables

Acronyms

CVD Chemical Vapor Deposition *(p. 3)*

DC Direct Current *(p. 14)*
DLVO Derjaguin–Landau–Verwey–Overbeek *(p. 16)*
DOS Density of States *(p. 11)*

EDL Electrical Double Layer *(p. 15)*
EDS Energy Dispersive X-ray Spectroscopy *(pp. 23, 24)*
EPD Electrophoretic Deposition *(pp. 1, 14, 17, 25, 30, 32, 35, 44, 45, 48, 49, 56)*
ER Evaporation Rate *(p. 62)*

FAT Fixed Analyzer Transmission *(pp. 21, 28)*
FWHM Full Width at Half Maximum *(pp. 61, 63–66)*

HL-LHC High Luminosity - Large Hadron Collider *(pp. 2, 35)*

IMFP Inelastic Mean Free Path *(pp. 8, 22)*

LESS Laser Engineered Surface Structure *(p. 3)*
LHC Large Hadron Collider *(p. 2)*
LIPSS Laser-Induced Periodic Surface Structures *(p. 3)*
LTCVD Low-Temperature Chemical Vapor Deposition *(p. 3)*

NEG Non-Evaporable Getter *(p. 3)*

RF Radio Frequency *(pp. 1, 48)*

SEE Secondary Electron Emission *(pp. 1, 5)*
SEM Scanning Electron Microscope *(pp. viii, x, xi, 22, 23, 33, 43, 56, 57, 59, 71, 72)*

SEY Secondary Electron Yield *(pp. 2–4, 6, 9, 11, 12)*

SN Signal-to-Noise *(pp. 18, 36)*

TEY Total Electron Yield *(pp. vii, ix–xii, 1–4, 6–9, 11, 27, 28, 30–33, 35–37, 39–46, 48, 49, 68–70)*

UPS Ultraviolet Photoelectron Spectroscopy *(p. 49)*

XPS X-Ray Photoelectron Spectroscopy *(pp. viii, 1, 19–22, 25, 33, 34, 46, 48, 49, 63–67)*

XRD X-Ray Diffraction *(pp. x, 58, 59)*

1 Introduction

High Total Electron Yield (TEY) materials have long posed challenges in both scientific and engineering domains, as phenomena such as multipacting and electron cloud formation disrupt the proper functioning of Radio Frequency (RF) devices in space, leading to reliability reduction, power losses, and device failures, and inhibiting the development of high-luminosity, stable positively charged beams in particle accelerators [2–6].

Electron cloud formation negatively impacts the operation of particle accelerators. During accelerator operation, the high-energy beam can ionize the residual gas inside the chamber, ejecting energetic electrons toward the walls. Additionally, when the beam is deflected, it emits synchrotron radiation, which induces photoelectron emission when photons irradiate the walls. When the generated electrons strike the walls, several energy loss mechanisms are triggered, leading to the production and emission of secondary electrons, a process known as Secondary Electron Emission (SEE). Although these secondary electrons have energies below 50 eV, they can be accelerated by the passing beam. Since the beam consists of bunches of positively charged particles with a 25 ns bunch spacing [7], the secondary electrons experience attractive electrostatic forces, gaining kinetic energy. Once the bunch has passed, the electrons drift towards the wall, acting as a new primary electron. The process can repeat, generating additional electrons, and leading to an exponential multiplication (multipacting effect). Consequently, pressure and temperature rise inside the vacuum chamber [5]. In particular, the temperature rise disrupts the operation of superconducting magnets, responsible for bending the beam, whose resistivity depends strongly on temperature. The beam's quality is also degraded due to the electron cloud, which will electrostatically interact with it.

Due to the increasing requirements that future accelerators and applications are imposing, the purpose of this work is to study the secondary electron emission properties of free-standing N-doped graphene powder, as a potential solution, as well as the material's advantages compared with undoped graphene deposited onto a copper substrate by Electrophoretic Deposition (EPD). These comparisons are made by measuring the total electron yield. Surface characterization will also be carried out via XPS to evaluate the electronic structure and its influence on the material. In addition, a simplified version of

Taguchi's method will be applied to determine the optimal deposition parameters and to analyze them independently.

This project was carried out in the Surface Science and Vacuum Technology Lab at the Centro de Física e Investigação Tecnológica (CEFITEC) in collaboration with the Instituto de Plasmas e Fusão Nuclear (IPFN), which produced and supplied the graphene and N-doped graphene powders.

1.1 State of the Art

The effect of electron cloud formation was first observed in the late 1960s in the Novosibirsk medium-energy proton storage rings [8]. At that time, it was regarded as a phenomenon of limited significance. However, as demands on beam energy and intensity increased, it became a major obstacle in accelerator physics. At CERN, in 1977, that phenomenon was observed during an operation with bunched proton beams in the Intersecting Storage Ring (ISR). As the chambers were made of aluminum, a sudden pressure rise was recorded for a specific combination of bunch charge and bunch spacing. Oswald Gröbner attributed this effect to the high Secondary Electron Yield (SEY) of aluminum and named the mechanism bunch-induced multipactoring. In 2018, the Chair of the Large Hadron Collider (LHC) Machine Advisor Committee emphasized that "LHC electron cloud is a top priority for the LHC and for CERN" following the challenges encountered during LHC Run 2, when the accelerator operated close to cryogenic limits in some arcs. When extrapolated to the upgraded system, named High Luminosity - Large Hadron Collider (HL-LHC), the heat load generated under these conditions would be unacceptable for high-load sectors [7]. This reinforced the need to develop effective strategies to mitigate secondary electron emission from the chamber walls.

While pure metals inherently exhibit low TEY, exposure to air causes surface oxidation, which significantly increases TEY. To address this, cleaning processes such as plasma discharge and bake-out are critical for minimizing electron cloud formation. However, these methods do not prevent recontamination during prolonged air exposure, which occurs during maintenance periods [2]. Since accelerators are primarily constructed of copper, aluminum, or stainless steel, numerous approaches have been explored over the years to reduce the TEY of these materials, with surface modification emerging as the principal focus. These approaches can be categorized as follows:

- Altering the surface composition by depositing a low TEY coating on the inner walls of the accelerator.
- Modifying surface roughness to suppress secondary electron emission.
- Utilizing the dose effect to induce surface changes through electron bombardment.

Although all these methods effectively reduce TEY, not all are practical for accelerator applications. Applying low TEY coatings and leveraging the dose effect are the most commonly employed strategies due to the difficulty of altering surface morphology on a large scale in a sustainable manner. Nevertheless, recent advancements at CERN, such as the development of a robot capable of modifying surface topography along the accelerator, have made morphological changes more feasible. This robot utilizes Laser Engineered Surface Structure (LESS) technology, which employs laser pulses (ranging from nanoseconds to picoseconds) to ablate material and create nanorough surfaces. More recent investigations have also explored femtosecond laser pulses to fabricate Laser-Induced Periodic Surface Structures (LIPSS)[5].

Among these approaches, applying a thin film over a surface is considered the most effective method for reducing TEY. The primary challenge of this method has been identifying a material that is vacuum-compatible, chemically inert, and resilient against air exposure, while maintaining its properties over time. Graphitic amorphous carbon coatings have been explored as low SEY candidates, as only conductive materials exhibit sufficiently low SEY. In parallel, CERN also developed Non-Evaporable Getter (NEG) coatings to pump regions with unfavorable geometry for conventional pumping techniques. A typical solution is the TiZrV alloy, which not only provides high pumping speed, but also has low TEY after the activation at about 160 °C for 48 h. These surfaces also help mitigate ion-induced pressure instability and background pressure due to their low stimulated gas desorption yield. NEG materials have a TEY of approximately 2.0 in their unactivated state, but this can drop to about 1.1 after two hours of baking at 200 °C. Moreover, their SEY remains relatively stable (within 0.1) after exposure to a flux of approximately 4 Pa·s of H_2, H_2O, CO, and CO_2. However, repeated air exposure progressively increases the maximum SEY to around 1.4 due to NEG deterioration, i.e., after the exposure for 7 times [9]. It is also important to note that NEG materials are only applicable to straight and bakeable sections of accelerators, as their activation temperature may interfere with the magnetic properties of bending magnets.

Graphene coatings have recently been investigated as a promising alternative due to their exceptional properties, including high mechanical strength, elasticity, chemical inertness, large specific surface area, and low SEY (ranging from 0.5 to 1.0) [10]. Graphene samples can be produced using various techniques, such as Chemical Vapor Deposition (CVD) [11]. While CVD is scalable for large-scale applications, it typically requires high temperatures, which are unsuitable for accelerators. A more recent development, Low-Temperature Chemical Vapor Deposition (LTCVD), offers promise as a viable solution, though it is not yet reliable enough for widespread application [12]. In order to deposit high-quality free-standing graphene powder at relatively low temperatures, the electrophoretic deposition technique is adopted in this work, which will be further discussed in detail later.

Concerning surface roughness, this approach has been extensively studied to explore low TEY surfaces. In roughened materials, secondary electrons are more likely to strike

surface protrusions, where their low energy reduces the likelihood of further secondary electron emissions, thereby lowering the material's overall electron yield [5]. Techniques employed to generate grooves include laser ablation (as mentioned earlier), wet etching (using acid solutions on metallic substrates) [13], and the application of these techniques to thin-film coatings. Combining surface roughness modifications with graphene coatings could further enhance the reduction of SEY.

The final approach, called the dose effect, leverages the electron cloud phenomenon induced by positively charged beams in accelerators. This effect uses the electron cloud effect to bombard the surface with energetic electrons. The surface has to be contaminated by hydrocarbons. Over time, the surface composition and structure of the carbon-based surface layer are modified into a graphitic amorphous structure, which has low TEY. For instance, electron bombardment can increase the relative carbon surface content from 40 % to 60 %, as reported in [6]. Although the exact origin of the carbon is uncertain, it is hypothesized to stem from the material itself, adsorption from residual gases, or hydrocarbon contamination [4]. The dose effect has been shown to reduce SEY to around 1.2, making it a valuable complementary method for achieving a low SEY surface.

Furthermore, studies have demonstrated that nitrogen-doped (N-doped) graphene exhibits even lower maximum SEY values compared to the undoped graphene under similar conditions. Reported maximum SEY values for N-doped graphene range between 0.84 and 0.96 (depending on the doping percentage), while undoped graphene exhibits a SEY of approximately 1.0, as reported in [14].

2

Theoretical Concepts

2.1 Secondary Electron Emission - SEE

Secondary Electron Emission (SEE) refers to the phenomenon in which a solid surface emits electrons following the impact of primary electrons. In reality, the emitted electrons are originated from different processes. They can be elastic or inelastic backscattered electrons, or true secondary electrons, which are generated within the material. These classifications are typically distinguished by their kinetic energy. However, particles cannot be distinguished from each other. Electrons with kinetic energy below 50 eV are generally classified as true secondary electrons [15].

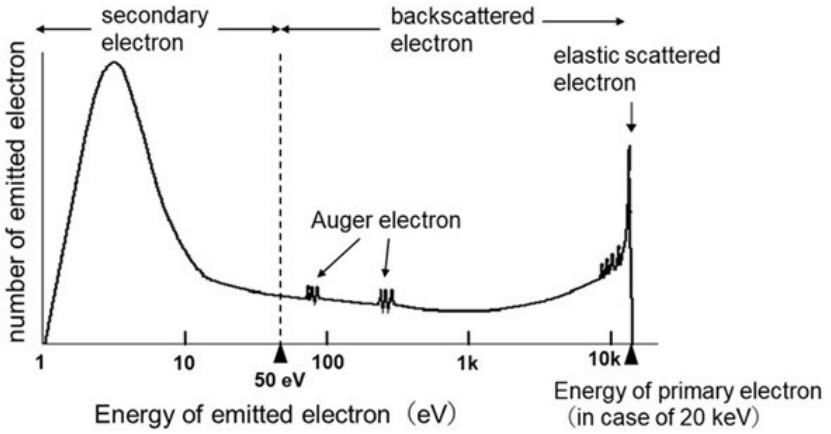

Figure 2.1: Energy spectrum of emitted electrons (adapted from [16]).

The generation of true secondary electrons involves three main stages [17]:

1. Production of internal secondary electrons.
2. Transport of these electrons through the bulk material toward the surface.
3. Emission through the solid–vacuum interface.

When a primary electron penetrates the surface, it begins to lose energy due to interactions with the material's electrons. This energy loss occurs through elastic and inelastic

collisions or via plasmon excitations, which are quantified by the collective oscillation of the electron cloud within the solid.

As a result of this energy transfer, some internal electrons, typically those near the surface, may acquire enough kinetic energy to overcome the vacuum level. However, during their transport to the surface, these electrons undergo further energy loss, often through the same mechanisms. Since secondary electrons possess significantly lower kinetic energy compared to primary electrons, the relative contributions of different processes will differ for secondary and primary electrons.

Finally, once secondary electrons reach the solid–vacuum interface, they will only be emitted if their momentum component normal to the surface is sufficient to overcome the surface potential barrier. If not, despite having kinetic energy above the work function, the electrons may still be reflected into the material.

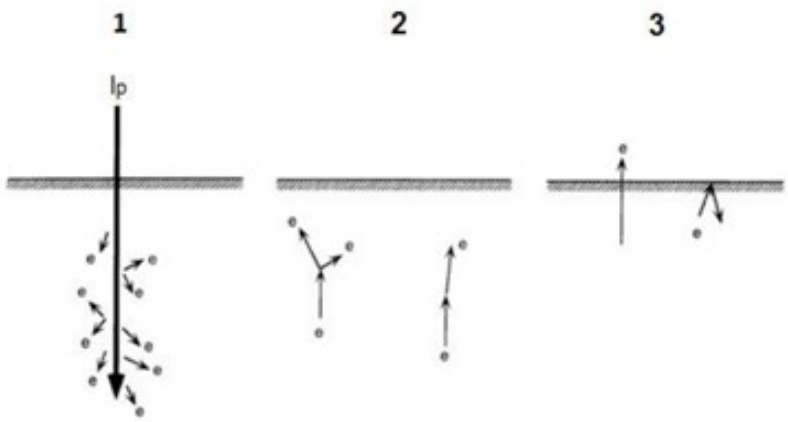

Figure 2.2: Steps for productions of true secondary electrons, adapted from [18].

2.1.1 Secondary Electron Yield - SEY

To mitigate electron cloud formation, it is crucial to quantify the number of electrons emitted from a given material. In practice, the measurement of this emission involves detecting the total emitted current, which includes elastic and inelastic backscattered electrons, as well as true secondary electrons.

When focusing specifically on low-energy secondary electrons, the Secondary Electron Yield (SEY) is defined as the ratio between the secondary electron current (I_s) and the primary electron current (I_p):

$$\delta = \frac{I_s}{I_p} \tag{2.1}$$

The key distinction between SEY and Total Electron Yield (TEY) lies in their sensitivity to the primary electron energy. TEY is significantly influenced by the energy of the incident electrons, particularly because backscattered electrons retain a substantial portion of the primary energy, either fully or partially [3].

2.1.1.1 Factors that influence TEY

The interaction between primary electrons and solid matter leads to the emission of secondary electrons across a range of energies. When these electrons retain energy close to that of the incident beam, they are classified as elastic backscattered electrons. In such cases, the primary electron interacts with the electrostatic field of atomic nuclei, resulting in scattering. Due to the significantly higher mass of the nucleus compared to the electron, the energy transfer is minimal, and the backscattered electron preserves nearly all its initial energy. This interaction can be described by the Rutherford scattering model, particularly for light elements and large scattering angles, where the shielding effect of atomic electrons is negligible.

Another elastic scattering mechanism arises from atomic vibrations within the crystal lattice, commonly referred to as phonons. These thermal vibrations can interact with the primary electrons, leading to energy exchange and deflection. However, since phonon energies are typically below 0.1 eV (on the order of k_BT), such interactions are still considered elastic. Phonon scattering is temperature-dependent and increases with the atomic number Z, like the elastic scattering, of the scattering atom as $Z^{3/2}$. Consequently, it is generally negligible for either light elements or low TEY materials, which are both the focus of this work.

In contrast, when the primary electron electrostatically interacts with the outer-shell electrons of atoms, energy is transferred to these internal electrons, resulting in inelastic backscattering. Unlike elastic scattering, the cross-section for inelastic scattering does not follow a simple power-law dependence on Z. Instead, it reaches a minimum for noble gases and a maximum for metals with one or two weakly bound valence electrons, where plasmon-related effects are more prominent.

If neglecting the excitation of core electrons, inelastic effects can be caused by both single-electron excitations and collective excitations, such as plasma resonances. In conductive materials, conduction band electrons may be excited to an unoccupied higher energy state, probably within the same band. In insulators and semiconductors, valence electrons require energy sufficient to overcome the bandgap and reach the conduction band. If the final energy state when the electron reaches the surface lies above the vacuum level, it may be emitted as a secondary electron.

When considering collective effects involving multiple atoms, inelastic scattering can induce oscillations in the valence electron density, giving rise to plasma resonance. This phenomenon can be modeled as a longitudinal traveling wave or described in terms of a quasiparticle, known as a plasmon. The energy of a plasmon is defined by:

$$E_p = \hbar\omega_p \tag{2.2}$$

where $\hbar$ is the reduced Planck constant and ω_p is the plasmon frequency. Due to the short lifetime of plasmons, they may decay by transferring their energy and momentum to a single electron, resulting in secondary electron emission via Landau damping.

The probability of energy loss by a primary electron by its interaction with matter depends on its kinetic energy. This relationship is described by the so-called universal curve, which is valid for energies between 1 eV and 10 000 eV above the Fermi level. One of the many empirical formulas for the Inelastic Mean Free Path (IMFP), λ_{m}, in monolayers, is expressed as [19]:

$$\lambda_m = \frac{538}{E^2} + 0.41(aE)^{1/2} \tag{2.3}$$

where E is the electron energy (in eV) and a is the monolayer thickness (in nanometers).

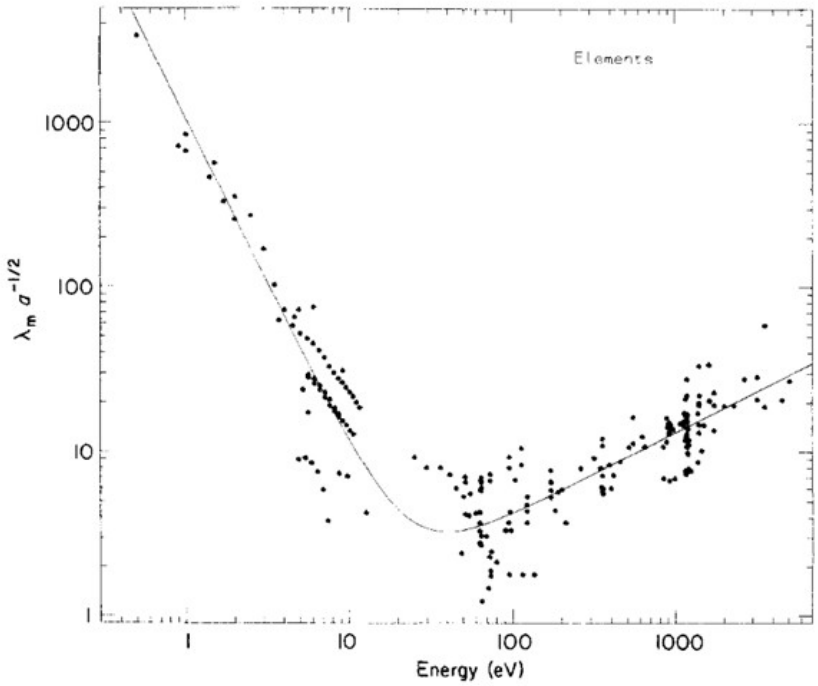

Figure 2.3: Compilation of results for IMFP as a function of electron energy, adapted from [19].

As can be seen in Figure 2.3, at low kinetic energies, the IMFP is relatively large, as the electron lacks sufficient energy to induce interband transitions or plasmon excitations. As the energy increases, electrons gain the ability to excite other electrons to higher bands and generate phonons, although phonons play a minor role in this work, given the focus on light elements. These transitions typically occur below 10 eV. Reaching the 10–30 eV range, corresponding to plasmon excitation energies, the IMFP reaches a minimum due to an increase in inelastic scattering cross-section due to both contributions. At even higher energies, the likelihood of plasmon formation and interband transitions decreases, as faster electrons spend less time interacting with the material [20].

In addition to the electron–matter interaction mechanisms, surface morphology significantly influences the TEY. On rough surfaces, secondary electrons are more likely to collide with surface protrusions. Due to their low kinetic energy, these electrons are less

likely to produce further emissions, thereby reducing the overall electron yield [5]. However, suppose the spatial frequency is too low. In that case, the TEY may increase because the primary beam is incident obliquely to the surface normal, which shortens the path that internal electrons must travel.

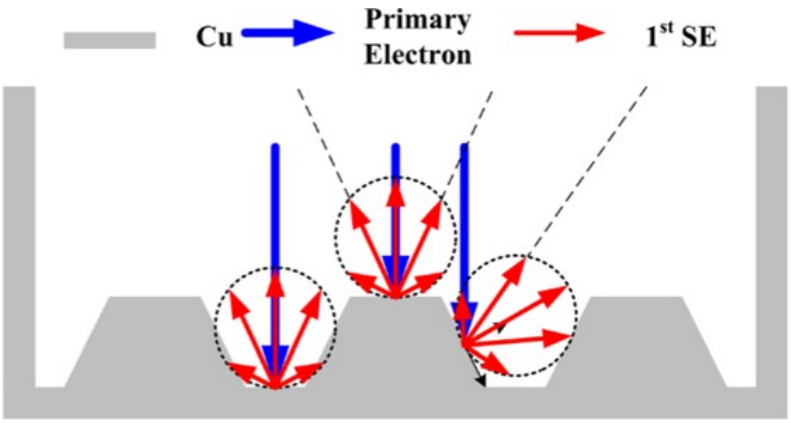

Figure 2.4: Angular dependence on secondary electron emission (adapted from [21]).

This effect is also evident in the shape of the SEY curve by the presence of a tail, visualized in the Figure 2.5. On rough surfaces, the descending slope beyond the SEY peak is more gradual compared to that of smooth surfaces.

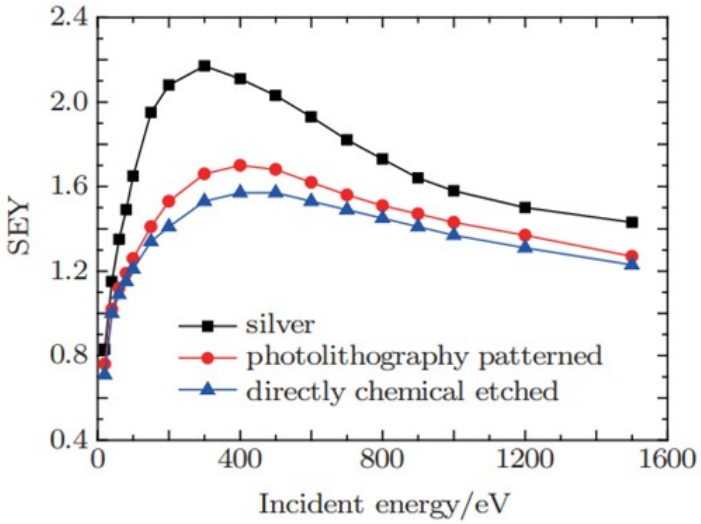

Figure 2.5: SEY curves of three different types of surfaces, adapted from [22].

This behavior is attributed to the attenuation of depth dependence in energy loss processes. On rough surfaces, secondary electrons do not require a momentum vector normal to the flat surface in order to escape. Instead, they may exit through the sides of surface features, increasing the likelihood of emission despite lower energies, similar to the increase in SEY observed as the primary beam angle increases, up to the point where backscattering becomes dominant [23].

2.2 Graphene

Graphene is a carbon-based material consisting of a single layer of carbon atoms arranged in a two-dimensional hexagonal lattice.

Carbon, with atomic number 6, is a tetravalent element, meaning it has four valence electrons available for bonding. In its ground-state electronic configuration, these electrons occupy the $1s^2$, $2s^2$, and $2p^2$ orbitals. However, to form more stable chemical structures, carbon atoms undergo hybridization. For instance, in diamond, one 2s electron is promoted to an empty 2p orbital, leading to the formation of four equivalent sp^3 hybrid orbitals arranged in a tetrahedral geometry where the bonds are as far as possible from each other.

In graphene, however, only two of the 2p orbitals participate in hybridization, forming three sp^2 hybrid orbitals that result in strong hexagonal in-plane covalent bonds. These bonds, known as σ bonds, are stronger than the C–C bonds found in sp^3-hybridized diamond.

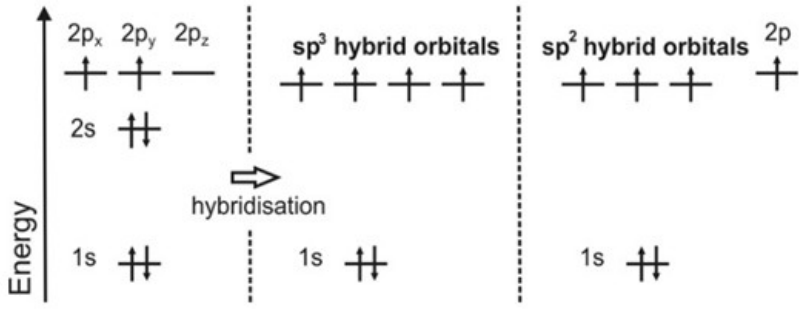

Figure 2.6: Atomic orbital diagram of a carbon atom, adapted from [24].

The remaining unhybridized 2p orbital, oriented perpendicular to the plane with hybridized orbitals, contributes to the formation of π bonds through overlap with adjacent π electrons from other carbon atoms. These π -bonds give rise to delocalized electronic states, forming the valence (π) and conduction (π*) bands. Using a simple nearest neighbor tight-binding approximation with one π electron per atom, the band structure of monolayer graphene can be described by the following dispersion relation:

$$E^{\pm}(k_x, k_y) = \pm\gamma_0\sqrt{1 + 4\cos(\frac{\sqrt{3}k_x a}{2})\cos(\frac{k_y a}{2}) + 4\cos^2(\frac{k_y a}{2})} \tag{2.4}$$

where a = $\sqrt{3}a_{C\text{-}C}$, and γ_0 is the nearest neighbor overlap integral, which takes a value between 2.5 and 3 eV.

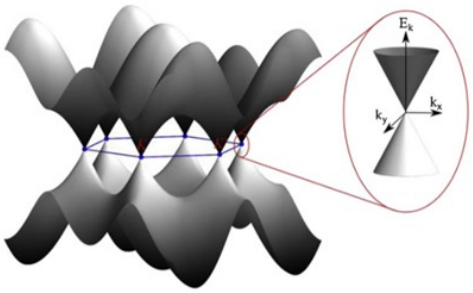

Figure 2.7: Band structure of graphene (adapted from [25]).

Each carbon atom contributes one electron to the valence band, while the conduction band remains unoccupied at 0 K. As it is possible to see in Figure 2.7, the two bands are "in touch" at the so-called Dirac points, through which the Fermi level passes. Near these points, the dispersion relation becomes linear:

$$E^{\pm}(k) = \hbar v_F |k - K| \tag{2.5}$$

Here, K represents the Dirac point in reciprocal space, located at $[\frac{2\sqrt{3}\pi}{3a}, \frac{2\pi}{3a}]$ or $[\frac{2\sqrt{3}\pi}{3a}, -\frac{2\pi}{3a}]$, and $v_F = \frac{\sqrt{3}\gamma_0 a}{2\hbar} \approx 1 \cdot 10^6$ m/s is the Fermi velocity. This band structure gives graphene unique electronic properties, such as pseudo-spin, relativistic-like charge carriers, and a vanishing carrier density at the Dirac points. This last feature characterizes graphene as a zero-gap semiconductor, with a vanishing Density of States (DOS) at the Fermi level [25].

Graphene's relevance in this work lies in its low secondary electron emission characteristics. As previously discussed, conductive materials typically exhibit low electron yields because excited internal electrons lose energy more efficiently via interactions with other valence electrons. The same mechanism applies to graphene, where energy is readily transferred to the delocalized π-electron system.

On the other hand, plasmon decay within the material will enhance secondary electron generation. Analysis of the electron energy loss spectrum reveals two prominent peaks in the ranges of 7–12 eV and 28–33 eV, corresponding to π and π+σ plasmons, respectively. The first peak results from collective oscillations of π electrons, while the second involves all valence electrons and appears more prominently in the spectrum [26]. One should expect that plasmonic oscillations contribute to the SEY.

2.2.1 N-doping Graphene

While pristine graphene is already an excellent candidate for reducing the TEY, doping it can further tailor its electronic properties. In particular, doping with nitrogen modifies the band structure, shifting the Fermi level to higher energies, above the Dirac points, as illustrated in the Figure 2.8.

Nitrogen doping affects secondary electron formation in two opposing ways:

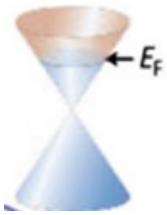

Figure 2.8: Fermi level shift by N-doping (adapted from [25]).

1. Reduction of π Electrons: When a carbon atom is substituted by nitrogen, one π electron is removed from the conjugated system. This reduces the material's electrical conductivity, which may lead to a higher SEY.

2. Suppression of Plasmon Formation: Nitrogen incorporation suppresses collective excitations, particularly the π plasmons, thereby reducing the probability of generating internal secondary electrons [14].

Despite the opposing effects, nitrogen doping generally leads to a reduction in secondary electron emission, as the suppression of plasmon-related excitations outweighs the slight conductivity loss from reduced π electron density, as reported in [14].

2.2.1.1 Nitrogen Bonding Configurations in Graphene

When nitrogen atoms are introduced into the graphene lattice, they can form several distinct bonding configurations. The five most common types are pyridinic, pyrrolic, graphitic, amine, and N-oxide nitrogen [27].

Pyridinic nitrogen

This configuration involves a nitrogen atom bonded via one σ bond to one carbon and both a σ and π bond to another carbon, within a hexagonal ring, where the nitrogen atom is sp^2-hybridized. Pyridinic nitrogen can introduce structural defects, as it fills the valence orbitals of its adjacent carbon atoms, potentially disrupting the delocalized π system.

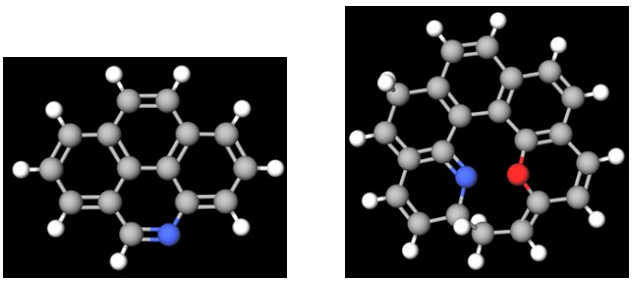

(a) (b)

Figure 2.9: Pyridinic bond configurations without a) and with b) vacancy.

Pyrrolic nitrogen

Here, nitrogen shares two σ bonds with neighboring carbon atoms, but due to its bonding geometry, the lattice is deformed, forming a pentagonal ring within the graphene

sheet. To complete its sp^2 orbital, nitrogen typically forms a third bond, often with hydrogen, making it a 3-coordinated bond. Like pyridinic nitrogen, pyrrolic configurations can introduce vacancies or holes, reducing lattice regularity.

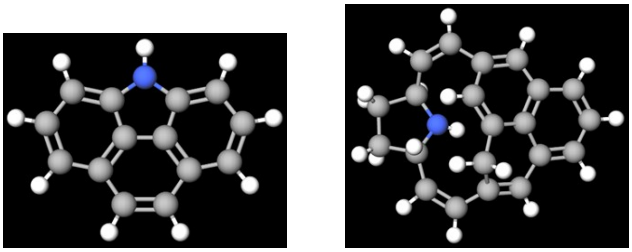

(a) (b)

Figure 2.10: Pyridinic bond configurations without a) and with b) vacancy.

Graphitic nitrogen

In this case, nitrogen replaces a carbon atom within the hexagonal lattice. While it maintains the planar structure, the loss of one π electron breaks aromaticity at that site. In some cases, this substitution can distort the lattice, leading to the formation of non-hexagonal rings, such as pentagons and heptagons [27, 28].

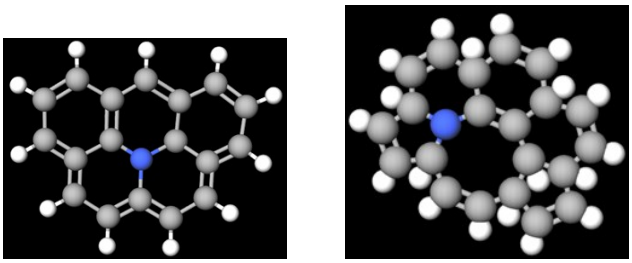

(a) (b)

Figure 2.11: Graphitic nitrogen bond configurations without a) and with b) lattice disruption.

Amine and N-oxide groups

These configurations involve nitrogen bonded to atoms other than carbon, typically hydrogen (amine) or oxygen (N-oxide). Due to the wide variety of bonding possibilities and molecular environments, only schematic representations of two common configurations are provided in the Figure 2.12.

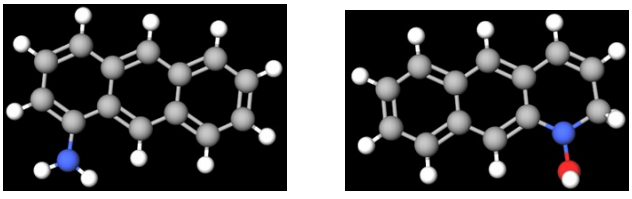

(a) (b)

Figure 2.12: a) Amine b) N-oxide.

2.3 Electrophoretic Deposition

Electrophoretic Deposition (EPD) is a versatile technique used to deposit charged particles, typically ranging from the micro- to nanoscale, onto electrically conductive substrates under the influence of a Direct Current (DC) electric field [29].

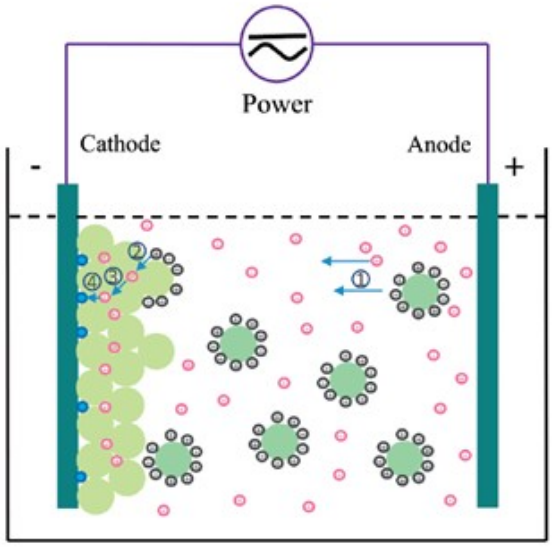

Figure 2.13: Electrophoretic Deposition schematic.

As outlined in [30], the process begins with the preparation of a stable suspension containing dispersed, independent particles. Ensuring suspension stability is crucial to prevent particle agglomeration due to Van der Waals forces. This is achieved by maintaining a low particle concentration and electrostatic stabilization, where a barrier is created that hinders the particles from coming into contact.

In the case of electrically neutral materials like graphene, charging the surface requires a solvent–electrolyte system capable of inducing surface ionization. The appropriate choice of solvent and electrolyte enables the adsorption or dissolution of oppositely charged ions, thereby establishing a surface charge through equilibrium processes.

Once a stable and charged suspension is prepared, a DC voltage is applied between two electrodes. The electric field drives the electrophoretic migration of charged particles toward the electrode with the opposite charge. Upon reaching the electrode surface, electrochemical reactions occur involving the ions surrounding the particles. These reactions facilitate both particle deposition and charge transfer between the electrode and the surrounding medium [31].

2.3.1 Particle model

When a solid particle is suspended in a polar liquid, it acquires a surface electric charge, which alters the local ion distribution in the surrounding medium. This interaction leads

to the formation of structured ionic layers around the particle, a phenomenon described by the Electrical Double Layer (EDL) model.

The most widely accepted representation of the EDL was initially proposed by Stern and later refined by Graham. According to this model, the counter-ions that neutralize the particle's surface charge form a compact layer adjacent to the surface, known as the Stern layer. Beyond this, additional ions are more loosely distributed, forming the diffuse double layer. The electrostatic potential difference between these two layers is referred to as the zeta potential (ζ).

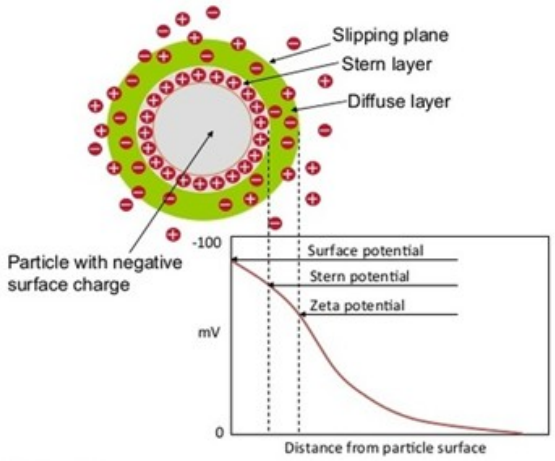

Figure 2.14: Electrical Double Layer and Zeta potential, adapted from [32].

The potential Ψ as a function of distance x from the particle surface decreases exponentially and can be described by:

$$\Psi = \Psi_\delta e^{-\kappa x} \tag{2.6}$$

Here, Ψ_δ is the Stern potential and κ is the Debye-Huckle parameter. The inverse of this parameter, $1/\kappa$, represents the Debye length, or the thickness of the double layer, i.e., the distance at which the potential falls to 1/e of its initial value at the Stern plane. This thickness can be represented by

$$\frac{1}{\kappa} = \left(\frac{\varepsilon \varepsilon_0 kT}{e^2 \sum_i n_i z_i^2} \right)^{1/2} \tag{2.7}$$

where e is the electric charge, n_i is the ions concentration with charge z_i, ϵ is the dielectric constant of the liquid and ϵ_0 is the permittivity of vacuum [33].

2.3.2 Particle mobility

The mobility of particles in a colloidal suspension under an electric field can be described in two distinct stages.

The first stage involves the initial movement of charged particles when exposed to the electric field generated between two electrodes, a process known as electrophoresis. The

electrophoretic mobility μ is defined as the ratio of the particle's velocity v to the applied electric field E:

$$\mu = \frac{v}{E} \tag{2.8}$$

Since this motion is driven by the zeta potential, Smoluchowski was the first to model the behavior of particles under a potential gradient, arriving at the following equation:

$$\mu = \frac{2}{3}\frac{\epsilon_0 \epsilon_r \zeta}{\eta} f(\kappa r) \tag{2.9}$$

where η is the solvent viscosity and $f(\kappa r)$ is the Henry coefficient, which depends on the core radius, r, which is the thickness of the double layer.

As deposition proceeds, the ions responsible for maintaining the particle surface charge also migrate toward the electrode. This leads to the formation of ionic layers that progressively shield the applied electric field, in a process analogous to the Debye shielding mechanism.

Under these conditions, diffusion becomes the dominant mechanism for particle transport once the particles are within a distance larger than a few Debye length from the electrode surface. However, as reported in several studies [33, 34], the contribution of diffusion is relatively minor, as deposition typically saturates within a few minutes.

2.3.3 Suspension stability

Ensuring the stability of colloidal suspension is a critical aspect of the electrophoretic deposition process. Suspension stability is primarily governed by the degree of particle dispersion, which, in turn, depends on the balance of interparticle forces.

The two dominant forces in colloidal systems are:

- Attractive Van der Waals forces;
- Repulsive electrostatic forces, which arise from the interaction between the diffuse layers of charged particles.

The equilibrium between these opposing forces determines whether particles remain dispersed or aggregate. According to the classical Derjaguin–Landau–Verwey–Overbeek (DLVO) theory, colloidal stability is determined by the total interaction energy (VT) between particles, given by the sum of the repulsive (VR) and attractive (VA) components:

$$V_T = V_R + V_A \tag{2.10}$$

The electrostatic repulsive component is described by:

$$V_R = \frac{\epsilon a \zeta}{2} \ln\left(1 + e^{-\kappa D}\right) \tag{2.11}$$

where ϵ is the dielectric constant of the liquid, a is the radius of the particle, ζ is the zeta potential of the particle, κ is the reciprocal of the double layer thickness, and D is the distance between two particles.

On the other hand, the Van der Waals attractive force is given by:

$$V_A = -\frac{aA_{131}}{2D} f(P) \tag{2.12}$$

where A_{131} is the Hamaker constant, which dictates the interaction between the particles and the medium, and f(P) is the retardation factor, raised by the electromagnetic characteristics of the Van der Waals dispersion forces [33].

2.3.4 Deposition parameters

The efficiency and quality of the EPD process are strongly influenced by several experimental parameters. In this work, the most relevant factors considered were deposition time, applied voltage, electrolyte concentration, and temperature.

Deposition time

Directly affects the thickness of the deposited layer. In general, longer deposition times result in thicker films. However, this relation is not linear: over time, the deposition rate tends to decrease due to field shielding effects inside the suspension and possible disruption of colloidal stability. Moreover, extended exposure to suspension, especially when it contains chemically aggressive components, can degrade the coating quality.

Applied voltage

As a key driver of deposition rate, it enhances the electric field strength and thus the mobility of charged particles [33]. Nevertheless, higher voltages can compromise film uniformity. As reported by [35], excessive electric fields give particles more kinetic energy, reducing their ability to settle properly on the substrate surface. This can lead to surface defects or non-uniform coatings due to particle impingement. Additionally, Negishi et al. observed that voltages above 100 V can induce n-propanol solvent breakdown, destabilizing the suspension and impairing the deposition process.

Electrolyte concentration

It plays a role similar to that of the applied voltage, since both influence the relation between the electric field and the surface charge of the particles, thereby determining their electrophoretic mobility. Besides that, the electrolyte concentration directly impacts the stability of the colloidal suspension. The concentration of ions in the medium regulates the thickness of the electrical double layer of particles, governing the repulsive electrostatic interactions between particles and of the electrodes, implying that too high concentrations lead to thinner layers, making it impossible to proceed with the particles' deposition.

Temperature

Temperature influences multiple aspects of the deposition process. As seen in the electrophoretic mobility equation 2.9, mobility depends inversely on the solvent viscosity, which decreases with increasing temperature, thereby facilitating particle motion. In the diffusion-limited regime, elevated temperatures enhance diffusion rates, accelerating particle transport. Temperature also affects ionic properties such as ion solvation, electrolyte ionization, and ionic strength, all of which can significantly alter the behavior of the suspension [36].

2.3.5 Taguchi's Method

Taguchi's method is used to optimize the deposition process by identifying the most favorable combination of parameters. This approach relies on the construction of an orthogonal array, which balances accuracy with experimental cost. A properly designed orthogonal array ensures that, for any given level of a parameter, all levels of the other parameters are tested at least once. This systematic distribution allows the influence of each factor to be independently evaluated.

The analysis of the experimental response is carried out using the Signal-to-Noise (SN) ratio, calculated through the Taguchi Loss Function. The SN ratio is defined such that it is maximized at the optimal performance parameters. Depending on whether the characteristic under study is to be minimized or maximized, the SN ratio is given, rescpectively, by [37]:

$$SN = 10 \log \left(\frac{\overline{y}_i^2}{s_i^2} \right) \tag{2.13}$$

$$SN = 10 \log \left(\frac{s_i^2}{\overline{y}_i^2} \right) \tag{2.14}$$

where

$$\overline{y}_i = \frac{1}{N_n} \sum_{u=1}^{N_n} y_{iu} \tag{2.15}$$

$$s_i^2 = \frac{1}{N_n - 1} \sum_{u=1}^{N_n} \left(y_{iu} - \overline{y}_i \right)^2 \tag{2.16}$$

represent the mean and variance of the performance characteristic for factor i, respectively.

After calculating the SN ratio for each sample, the average SN value is computed for each factor at each level. The relative influence of each deposition factor is then determined by evaluating the difference (Δ) between the highest and lowest average SN values for that parameter.

2.4 X-Ray Photoelectron Spectroscopy - XPS

X-ray Photoelectron Spectroscopy is a well-known technique used in surface science technology. It analyses the chemical composition and bonds within the surface of materials.

The technique is based on the photoelectric effect, wherein incident X-ray photons interact with a material, transferring energy to core-level electrons. If this energy exceeds the electron's binding energy relative to the vacuum level, the electron is ejected. By measuring its kinetic energy, the binding energy can be calculated using the fundamental photoemission equation:

$$E_b = h\nu - E_k - \phi \tag{2.17}$$

where E_b is the binding energy measured relative to the Fermi level, $h\nu$ is the incident photon energy, E_k is the measured kinetic energy, and ϕ is the work function of the spectrometer.

This general equation assumes a single-particle, ground-state system. However, when considering relaxation effects and interatomic interactions, a more detailed expression, incorporating both initial and final state effects, can be given by [38]:

$$E_b = -E_{HF} + V_{MP} + V_{VC} - E_{IA} - E_{EA} - \phi \tag{2.18}$$

where E_{HF} denotes the Hartree-Fock orbital energy of a free atom in vacuum. In this approximation, a single wave function is employed to describe multiple electrons to compute the orbital's energy. V_{MP} represents the shift in E_{HF} induced by Madelung potential when free atoms condense to form a solid. This shift arises from the influence of surrounding atoms in the lattice on the shell's potential [39] and is regarded as an initial state effect. V_{VC} corresponds to the shift in E_{HF} resulting from the presence of valence electrons. E_{IA} designates the intra-atomic relaxation energy, which originates from the shielding of the hole state (after ionization) by both the conduction electrons and the cores of neighboring atoms within a solid. E_{EA} refers to the extra-atomic relaxation energy. This contribution stems from the electron transfer to the core levels to attain the electrical equilibrium with the substrate [40].

The binding energy deviation, thanks to the presence of different neighboring atoms, is called the chemical shift. When these shifts are large enough, they appear as separate peaks in the spectrum.

If the instrument has sufficient resolution, it is also possible to observe fine structures in the core levels, such as spin-orbit splitting.

Analyzing the spectra obtained with this technique reveals different types of peaks, which correspond to binding energies and, in turn, to distinct chemical compounds. Beyond the primary photoelectron peaks, X-Ray Photoelectron Spectroscopy (XPS) spectra may exhibit several secondary features, such as shake-up, shake-off, and X-ray satellites, plasmons, charging effects, multiplet splitting, and Auger electrons.

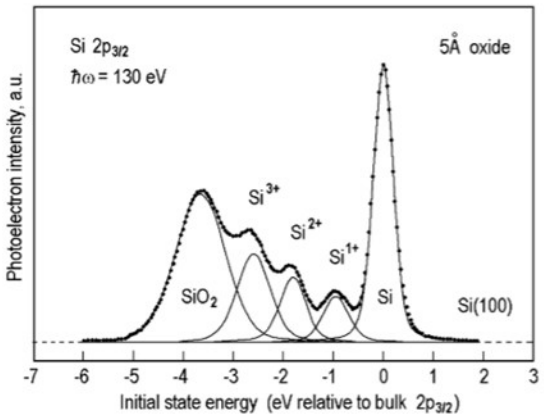

Figure 2.15: Example of chemical shift by an ultrathin oxide silicon layer on a silicon surface, adapted from [41].

The charging effect arises due to extra-atomic relaxation, as discussed earlier. Poorly conductive samples can accumulate positive charge during measurement, leading to peak shifts or broadening. As introduced in the section 2.1, plasmon losses occur when emitted electrons excite collective oscillations of conduction electrons. XPS can be used to quantify plasmon energy losses, making this another valuable application.

Shake-up satellites occur when the ionized atom is left in an excited state. Instead of all the photon energy going to a single core electron, a small part of it excites an atom's electron. Due to energy conservation, the photoelectron energy is lower, increasing the peak's binding energy. The shake-off satellites result from a similar process to shake-up satellites. In this case, the loss of photoelectrons' kinetic energy goes to an intraband transition, where the valence electrons go to a higher energy state.

On the other hand, X-ray satellites appear at lower binding energies and originate from non-monochromatic X-ray sources. In such cases, the X-rays usually have low intensity components with higher energies, producing photoelectrons with correspondingly higher kinetic energies, following the photoemission equation.

The multiplet splitting appears in atoms with unpaired electrons, particularly in transition metals. Those electrons can couple with an unpaired electron in a core level after photoionization, creating several new final states in which are known as multi-peak envelopes when observed in the following spectrum [42].

After the photoemission of a core electron, an outer-shell electron may transit to fill the vacancy. The energy released during this process can either be emitted as a photon or be transferred to another electron, which is then ejected as an Auger electron. Unlike photoelectrons, the kinetic energy of Auger electrons does not depend directly on the incident photon energy. Instead, it is determined solely by the energy levels of the atom involved, given by:

$$E_{KL_1L_{2,3}} = E_K - E_{L1} - E_{L2,3} - \phi \tag{2.19}$$

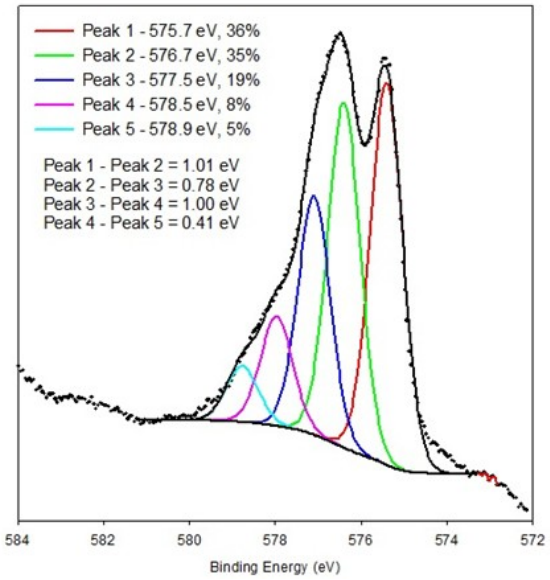

Figure 2.16: Multiplet structure of Cr $2p_{3/2}$ as an example, adapted from [43].

where $E_{KL_1L_{2,3}}$ is the kinetic energy of the Auger electron, E_K is the binding energy of the initial core level, E_{L_1} is the energy level of the electron that fills the vacancy, and $E_{L_{2,3}}$ is the energy level of the electron that is emitted as an Auger electron.

2.4.1 XPS Instrumentation

For surface analysis, ultra-high vacuum conditions of approximately $3{\cdot}10^{-8}$ mbar are required, achieved by an ion pump. This ensures a clean surface and minimizes interactions between X-ray photons, photoelectrons, and residual gas molecules. Under these conditions, X-ray photons are generated by a non-monochromatic dual-anode Al/Mg X-ray source [44], inducing the emission of photoelectrons from the sample. These photoelectrons then pass through a concentric hemispherical analyzer operating in Fixed Analyzer Transmission (FAT) mode. This mode only allows photoelectrons with a certain kinetic energy, after retardation by the entrance lens, to pass through the analyzer.

This analyzer features two metallic hemispheres: the outer and inner hemispherical electrodes are negatively and positively biased relative to the potential in the center of the analyzer, respectively, allowing only photoelectrons with specific energies to pass through the entrance and exit slits.

2.4.2 XPS Quantification

XPS is not only a powerful tool for identifying the chemical species present on a sample's surface, but it also enables quantification of their relative amounts through the analysis of peak intensities in the spectrum. The general expression for the intensity of a photoelectron peak from a core level of atomic species i is given by [41]:

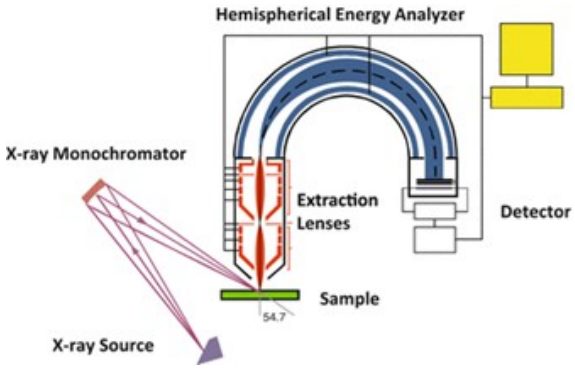

Figure 2.17: XPS experimental set-up, adapted from [45].

$$I_i = J_X \cdot \sigma_i(h\nu) \cdot \Delta t \cdot A \cdot T \cdot \int_{\gamma=0}^{\pi} \int_{\varphi=0}^{2\pi} L_i(\gamma) \int_{z=0}^{\infty} n_i(z) \cdot e^{-\frac{z}{\lambda \cdot \cos\theta}} \, dz d\varphi d\gamma \tag{2.20}$$

where J_X is the X-ray beam intensity, $\sigma_i(h\nu)$ is the photoelectron cross-section of the core level, Δt is the acquisition time, A is the area seen by the detector, T is the electron detection efficiency of the spectrometer, $L_i(\gamma)$ is the angular dependence of photoemission, γ is the angle between the incident X-ray beam and the direction of the ejected photoelectron, $n_i(z)$ is the atomic concentration as a function of depth z, θ is the take-off angle of the photoelectrons measured with respect to the surface normal, and λ is the IMFP length. To measure the thickness of samples using XPS, the most relevant parameter is the attenuation length, L, which is proportional to the photoelectron's kinetic energy ($E_{k,i}$) and material dependent [46, 47].

$$\lambda_i = K_m aterial E_{k,i}^{0.7} \tag{2.21}$$

The exponential term in the equation represents the attenuation of the signal with depth, meaning that the probability of detecting photoelectrons decreases exponentially as their origin lies deeper within the material. This is the reason why XPS is a surface-sensitive technique, typically probing only the top 1–10 nm of a sample.

For practical purposes, a sensitivity factor S_i is introduced to simplify quantification. The atomic concentration of species i within the same matrix can then be expressed as:

$$C_i = \frac{\frac{I_i}{S_i}}{\sum \frac{I_j}{S_j}} \tag{2.22}$$

where the denominator accounts for all elements j present in the material.

2.5 Scanning Electron Microscope

The Scanning Electron Microscope (SEM) technique is widely used to examine microstructure morphology and chemical composition by detecting various signals emitted from a

surface upon the incidence of a high-energy electron beam. The electron beam is typically produced by a field emission gun, as this source provides high brightness and very low divergence, thereby reducing the chromatic aberrations and allowing the beam to be focused into a small probe size. This enables high-resolution imaging in SEM.

Once the electron beam interacts with the sample surface, several types of signals are produced, as described in the 2.1 section, which includes true secondary electrons and backscattered electrons, but also characteristic X-rays and X-ray continuum radiation. By scanning the surface with the focused electron beam, the emitted secondary electrons are collected to generate topographic contrast, allowing the visualization of surface texture and roughness. Since secondary electrons are emitted with low kinetic energy, their escape depth is limited to a few nanometers, resulting in high lateral resolution, typically on the order of 10 nm, since they originate mainly from a small area near the surface.

The image contrast arises from variations in the intensity of secondary electrons reaching the detector. Bright regions in the image correspond to areas with high secondary electron emission, whereas darker regions indicate a lower detected signal. This occurs because surface protrusions can block the emission of electrons from nearby regions, causing features such as pits or depressions to appear darker. Conversely, elevated features such as peaks and hillocks appear brighter, as their geometry prevents emitted electrons from being recaptured by the surrounding structure. The relative positions of the detector, sample, and incident beam also influence image formation due to differences in the interaction volume.

The backscattered electrons are used primarily to produce images with enhanced chemical composition contrast, particularly when elements with significantly different atomic numbers are present. Heavier elements have more highly charged nuclei, leading to a greater probability of elastic scattering compared to the lighter elements. Because backscattered electrons retain most of their initial energy after interacting with the sample, they have a lower probability of being absorbed. However, this also results in lower lateral resolution, typically around 1 μm, when compared to secondary electron images, as well as lower signal intensity.

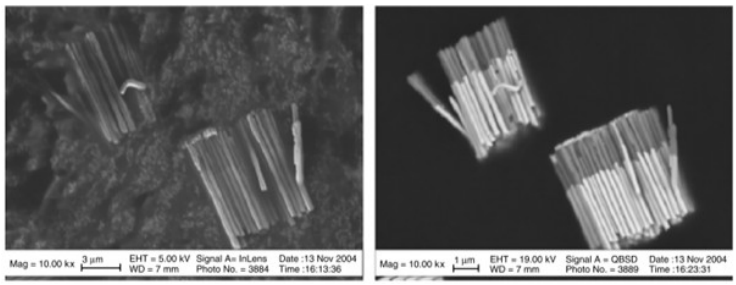

Figure 2.18: Ni/Au nanorods images formed secondary electron signal and backscattering electron signal, respectively, adapted from [48].

On the other hand, characteristic X-rays are mainly employed for Energy Dispersive X-ray Spectroscopy (EDS) rather than for image formation. After the incident electron beam

interacts with the atom, a core vacancy is created in an inner shell, following ionization. An electron from a higher-energy shell then fills this vacancy, emitting a photon with a well-defined energy during the relaxation process. In addition, incident electrons can undergo inelastic scattering, losing part of their energy and emitting photons. Since this process produces a continuous spectrum rather than discrete energies, these photons are referred to as continuum or Bremsstrahlung X-rays and usually contribute to background noise [48]. EDS uses a solid-state detector, typically a silicon drift detector, to collect and analyze the characteristic X-ray photons emitted from a sample. When these photons interact with the detector, they generate an electron-hole pairs. An electric field, established by an electrode at the detector surface, causes the electrons to drift towards a central collecting anode. The resulting charge pulse is converted into a voltage step, proportional to the X-ray energy. Higher energies produce a larger number of charge carriers, leading to higher voltage amplitudes. Each voltage step caused by one X-ray photon is then sorted into a histogram at a position corresponding to the step height. The accumulation of these events forms a complete X-ray energy spectrum [49].

3

Experimental Procedure

3.1 Deposition of the graphene coatings

Free-standing graphene and N-doped graphene powders were deposited onto copper substrates using EPD. The powders were produced by the low-temperature plasma group at IST, in atmospheric microwave plasma, providing high purity and low concentration of defects in the pristine material. The details of the graphene production can be found in Annex I. The copper substrates were cut from a 0.3 SF-Cu (Phosphorous-Deoxidized Copper) copper sheet into 20x10 mm^2 pieces with a 2.5 mm diameter hole for the electrical contact and the mechanical support. The counter electrode, made of gold, was fabricated with the same specifications. These dimensions were chosen to ensure compatibility with the XPS sample holders and to allow straightforward mounting in the EPD apparatus.

Since the deposition setup had to be assembled, a custom holder for the wires was designed in Autodesk Fusion and 3D printed. Copper wires were inserted through the smaller holes, and both the copper and gold substrates were screwed to the wires. The larger hole served as a vent for the corrosive chlorine gas (Cl_2) generated during the deposition. The entire setup was assembled in a glass beaker.

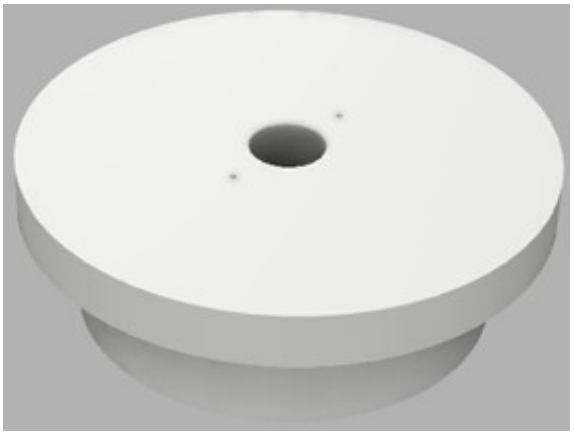

Figure 3.1: 3D model of the custom holder.

Before each deposition, the copper substrates were mechanically polished to remove

the oxide layer, followed by immersion in isopropanol under ultrasonic agitation for 9 minutes to eliminate debris and common surface contaminations. In parallel, the colloidal suspension was prepared from isopropyl alcohol as the solvent, and an aqueous solution with 33% mass fraction of HCl as the electrolyte. The required volumes depended on the deposition parameters, as the electrolyte-to-solvent ratio determines the ionic concentration. Typically, 2–2.5 mg of graphene powder was dispersed in the solution, which was then subjected to ultrasonic agitation to ensure, at least, suspension stability in the deposition initial state.

After preparation, two crocodile cables were connected to the wires, fixed on the substrates, enabling the application of a potential difference across the electrodes and thus generating the electric field inside the solution. At first, the effect of temperature was disregarded, however, subsequent findings highlighted its importance as a critical deposition parameter. To control it, the beaker was rolled up with a house regulating the temperature using a thermal bath.

For N-doped graphene, an additional ultrasonic step was introduced during the deposition, as this powder tends to aggregate more rapidly than pristine graphene and, in some cases, requires longer times to deposit effectively.

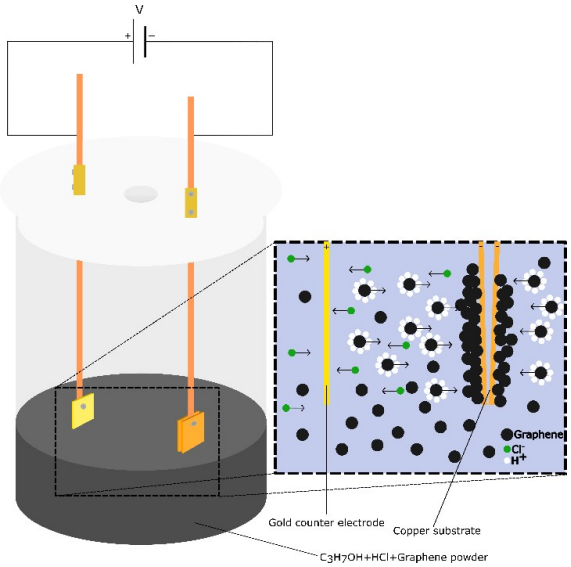

Figure 3.2: Schematic representation of EPD.

3.1.1 Parameter Optimization

The optimization process focused on three deposition parameters: the applied voltage, the electrolyte concentration, and the temperature. To achieve the best response while accounting for the main factors influencing the system, an experimental design approach was adopted. Specifically, a modified Taguchi method was employed, as it allows reducing production costs while targeting a mean performance close to the desired outcome.

The implementation of Taguchi's method followed several stages:

1. Construction of a Taguchi orthogonal array.

2. Determination of the effect of each variable on the output by minimizing the Taguchi Loss Function.

3. Calculation of the average signal-to-noise ratio for each factor and respective level.

4. Definition of the influence of each parameter on the overall process.

In the case of this work, three deposition parameters, HCl volume, Voltage, and temperature, were considered, each with four levels, as seen in Table 3.1. An array with this configuration was selected to achieve reliable conclusions while minimizing interference among the parameters. The corresponding array is shown below:

Samples	**HCl volume (μL)**	**Voltage (V)**	**Temperature (°C)**
1	40	20	16.0
2	40	30	18.5
3	40	40	21. 0
4	40	50	23.5
5	60	20	18.5
6	60	30	16.0
7	60	40	23.5
8	60	50	21.0
9	80	20	21.0
10	80	30	23.5
11	80	40	16.0
12	80	50	18.5
13	100	20	23.5
14	100	30	21.0
15	100	40	18.5
16	100	50	16.0

Table 3.1: Taguchi Orthogonal Array used in this work.

3.2 TEY Measurement

The TEY measurement apparatus consists of a cylindrical Faraday cup with an opening at the top and a sample holder mounted on its bottom, and a suppression electrode on the top, biased at -9 eV. An electron gun is positioned above the cup to direct the electron beam perpendicularly onto the sample surface. The beam energy was varied from 40 to 100 eV in steps of 20 eV, and from 100 to 995 eV in steps of 50 eV. A suppression electrode is negatively biased at the top, repelling secondary electrons to improve the measurement accuracy.

The TEY measurement is conducted in two stages:

1. Primary Electron Current Measurement: In this phase, the sample holder and cup are electrically connected. This configuration ensures all secondary and backscattered electrons are included in the current measurement, with no loss of electrons.

2. Secondary Electron Current Measurement: In the second phase, the sample holder is negatively biased at -5 eV, forcing secondary electrons to leave the surface and strike the cup walls. The current measurement now includes only these secondary and backscattered electrons.

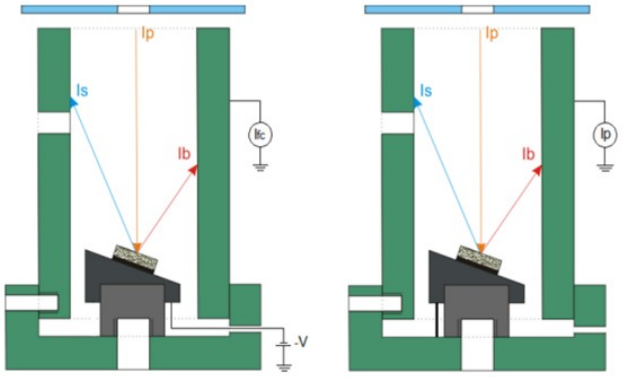

Figure 3.3: TEY typical apparatus. On the left side, secondary electron current is being measured, and on the right side, only the primary electrons are being detected (adapted from [18]).

For data acquisition, a switch was implemented to alternate between the measurement of the primary and secondary currents. The primary current sometimes has a drift over time, which affects the TEY measurement since I_s and I_p cannot be measured simultaneously. This systematic error is overcome by measuring the primary current twice, once before and once after the secondary current measurement, using the same acquisition time. Consequently, the TEY calculation equation was adjusted accordingly:

$$\delta = \frac{I_s}{\frac{I_{p1}+Ip2}{2}} \tag{3.1}$$

3.3 XPS Apparatus

To introduce a sample into the analysis chamber, it is first placed in a load-lock chamber. There, a diaphragm pump serves as the primary pump, followed by a turbomolecular pump to achieve high vacuum. Once this level is reached, the sample is transferred into the analysis chamber. The applied voltages, on the energy analyzer, are controlled by a LabVIEW program, which enables the definition of energy and time steps for the pass energy, as well as the energy range for spectral acquisition.

For full-spectrum acquisition, the typical energy range is 0–1010 eV, covering the most intense lines of gold, carbon, oxygen, copper, nitrogen, and chlorine, along with the carbon and oxygen Auger peaks. In this case, a time step of 0.5 s and an energy step of 0.5 eV are chosen. The FAT mode is set to 44 eV. For higher resolution measurements of specific lines, a pass energy of 22 eV is used. The electrons passing through the exit slit are

multiplied by the channeltron. The obtained signal is then processed by the preamplifier and recorded by the data acquisition system.

3.3.1 Data analysis

Spectral processing and interpretation were performed using the software CasaXPS. There, it is possible to calibrate the spectral energy axis against well-known binding energy references. In this work, calibration was achieved by measuring the Au $4f_{5/2}$ and Ag $3d_{5/2}$ photoelectron lines before sample analysis.

The program also provides options for selecting the type of background subtraction and the line shape, both of which are crucial for ensuring consistency and comparability of fitting parameters across different studies. Among various background methods, the most widely adopted, and the one applied in this work, is the Shirley background. This method corrects the contribution of inelastic scattering to line intensity, producing a step-like background [50], while simultaneously minimizing the asymmetry required in the line shape.

The choice of the line shape depends on the element under analysis and the electronic structure of the material. In this work, the most frequently used is the Gaussian–Lorentzian (Voigt) line shape, denoted GL(x), where x ranges from 0 to 100. GL(0) corresponds to a pure Gaussian, while GL(100) corresponds to a pure Lorentzian profile. Asymmetric line shapes are typically employed in pure metals, due to coupling between the conduction band and the probed core level, introducing additional asymmetry [42].

4

Results and Discussion

This chapter contains the results obtained from the samples prepared with the EPD apparatus, described in the 3.1 section. Also, a summary table with every deposited and analyzed sample, used in this chapter, can be seen in the annex IV.4. A method for evaluating the preservation of graphene and N-doped graphene properties is by comparing the results obtained by EPD with those prepared by pressing the raw material onto an indium foil and then applying the same experimental techniques. It also includes the analysis of these samples using the characterization techniques addressed previously, followed by a discussion of the results derived from them.

Three different sets of samples were prepared. The first set consisted of deposited graphene powder, with a focus on evaluating their dependence on HCl concentration. The second and third sets were prepared using N-doped graphene, with each designed for a different purpose and set of deposition parameters. One was used to evaluate the effect of each deposition factor independently, supported by calculations performed with a Python script, while the other served to see how the deposition was affected by establishing a baseline that keeps two parameters fixed and varies the third.

The goal of this work is to deposit N-doped graphene into copper, employing EPD, and to conclude the potential advantages of using it instead of its non-doped form. A dedicated section is included to compare the two materials directly. Finally, the last subchapter discusses additional phenomena observed during the course of this research.

4.1 Graphene Deposition

To replicate the previous results and establish a baseline for N-doped graphene deposition, the experiments were first carried out with pristine graphene. The deposition parameters, such as HCl concentration and applied voltage, were varied in a controlled manner to assess their influence on the sample's TEY. However, due to unexpected and unknown issues during the samples' characterization, the data related to voltage variation proved unreliable.

For the HCl concentration study, the applied voltage was fixed at 40 V. The graph

below shows the variation of TEY and the sp^2-to-sp^3 ratio as a function of HCl volume in 37.5 mL of isopropanol:

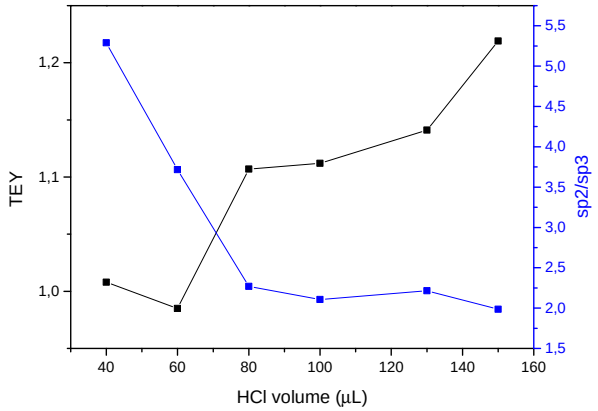

Figure 4.1: Effect of HCl content on TEY and sp^2-to-sp^3 ratio.

A clear trend is observed in the Figure 4.1: TEY increases with HCl concentration for values above 60 μL. This effect might arise because the electrolyte partially degrades the graphene sheets, forming C–Cl bonds with binding energies between 200.5 and 200.8 eV.

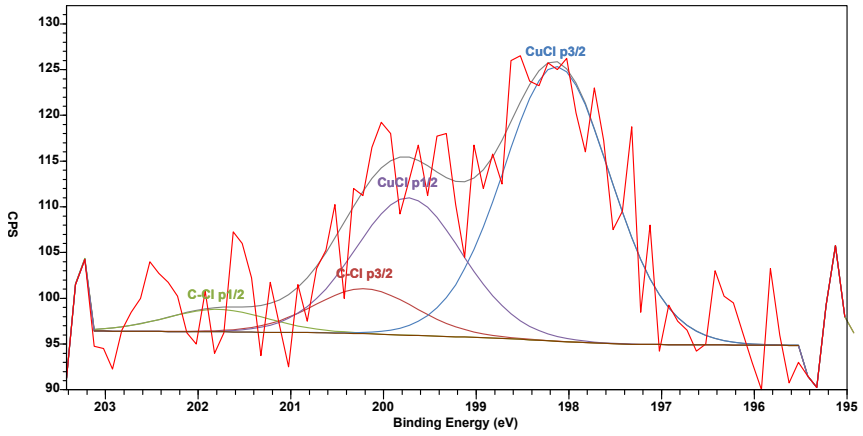

Figure 4.2: Cl 2p line peak fitting.

The Cl 2p line was fitted according to the binding energies reported in [51]. The spectrum 4.2 corresponds to the sample prepared with 150 μL of HCl. It reveals the presence of C–Cl bonds at 200.2 eV, $2p_{3/2}$, and Cu–Cl bonds, which are more prominent at 198.1 and 199.7 eV.

Moreover, since the deposited material is graphene, sp hybridization is not expected to originate from the graphene itself. The most plausible source is surface contamination from hydrocarbons. However, given graphene's chemical inertness, contamination from the powder itself is not considered as significant as from the solution. This becomes clearer when comparing the results to those of a pristine reference sample, prepared by compressing graphene powder onto an indium substrate. This sample is therefore used

as a benchmark, against which the best EPD result is compared:

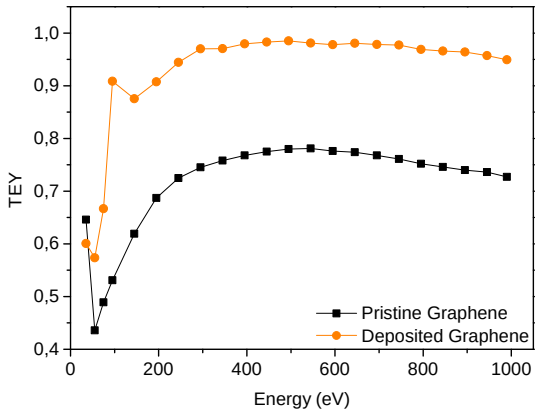

Figure 4.3: TEY as a function of the energy of the incident beam for Pristine Graphene and Deposited Graphene.

As shown in Figure 4.3, the lowest TEY obtained was 0.98±0.01, in which the applied voltage was 40 V and the HCl volume was 60 μL for 58 minutes. This result is lower than the value of 1.04, reported in a previous study using the same method, where the deposition parameters were 18 V and 50 μL of HCL for 30 minutes [3], due to the encounter of better deposition parameters and, possibly, to the usage of a different quality graphene powder. However, the benchmark value for the pristine reference sample was 0.78±0.01, with a sp^2-to-sp^3 ratio of 21.2, reinforcing the inert nature of the material.

In terms of atomic quantification, the pristine sample showed a very low oxygen content, again supporting this conclusion. Although the oxygen levels in deposited samples do not display a clear trend, it must be considered that some oxygen is bound to the underlying copper substrate, i.e., in a different matrix. For this reason, the sensitivity factors used in the quantification of carbon, oxygen, and chlorine require recalculations. Nevertheless, the sample deposited with 130 μL of HCl displayed a lower oxygen percentage than expected, complicating the establishment of a reliable relationship between oxygen content and TEY.

4.2 N-doped Graphene

The purpose of this work is to assess whether N-doped graphene provides advantages over pristine graphene when deposited by EPD. A direct comparison between the two materials allows evaluation of the potential improvements introduced by nitrogen doping.

TEY measurements 4.4 show that nitrogen doping has indeed effect on the maximum TEY, which decreased from 0.78±0.01 for pristine graphene to 0.72±0.01. However, for lower electron beam energies, between 40 eV and 200 eV, pristine graphene exhibits lower

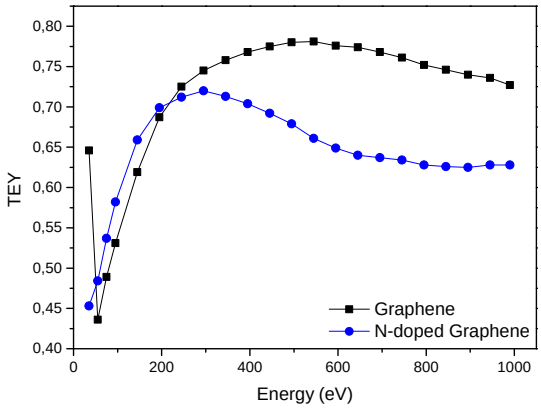

Figure 4.4: TEY as a function of the energy of the incident beam for Graphene and N-doped graphene.

TEY, while above 200 eV, N-doped graphene performs better. The low slope of both curves at high energies is a good representation of high surface roughness. Additional characterizations of the N-doped graphene samples by SEM and Raman spectroscopy, revealing its specific surface topography and the major features expected in graphene can be found in the Appendix A.

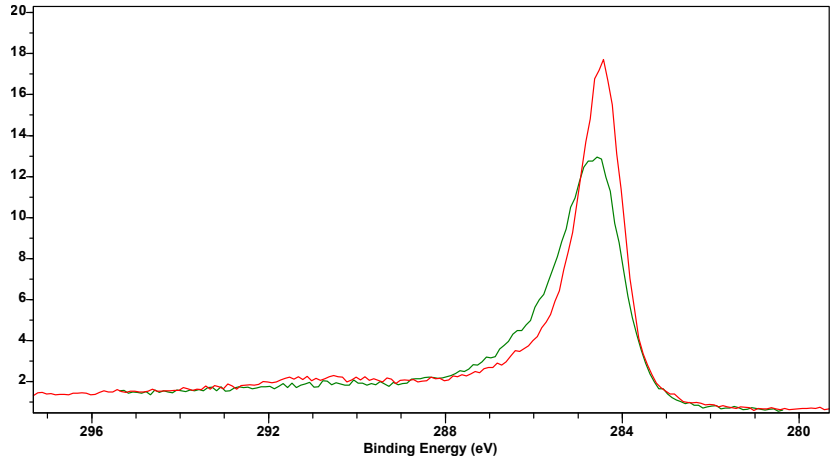

Figure 4.5: C1s line spectra: Green line - Graphene; Red line - N-doped graphene.

Overlaying the XPS C 1s spectra 4.5 highlights the effects of doping. Both peaks were averagely normalized using CasaXPS at 295.16 eV over a 2 eV width, ensuring the same baseline for comparison. The sp^2 carbon component appears at approximately 284.37 eV for both materials, enabling direct evaluation. Two key observations emerge:

1. The C 1s line of the N-doped graphene broadens relative to the pristine graphene. This can be attributed to chemical shifts of carbon atoms bound to nitrogen, as well as lattice distortions such as pentagon formation, especially in pyrrolic configuration, but also from the graphitic nitrogen.

2. A reduction in π-plasmon contributions is observed after doping with 3.5 %. The plasmon loss contribution to the C 1s line decreases from 4.19 % in pristine graphene to 2.12 % in the N-doped variant.

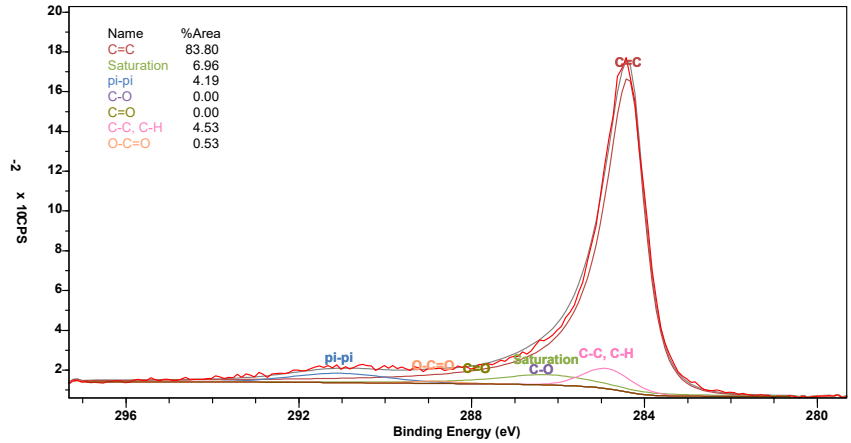

(a) Graphene.

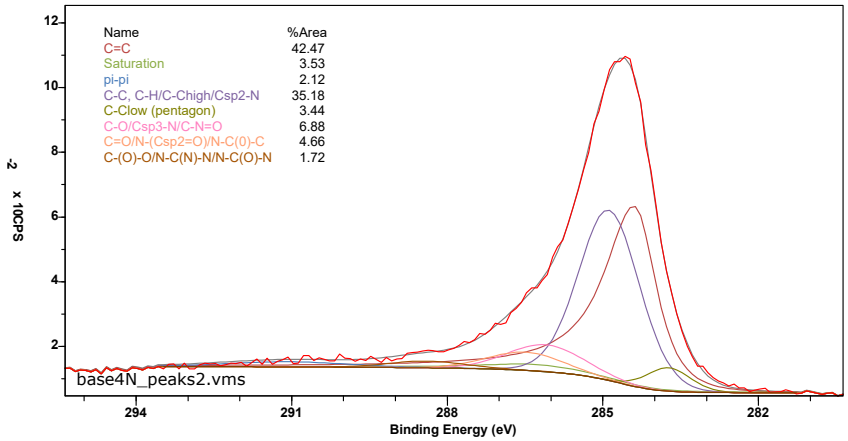

(b) N-doped graphene.

Figure 4.6: C 1s line peak fitting of (a) Graphene and (b) N-doped Graphene.

From the fitting of two spectra, a small peak emerges at lower binding energies, which can be associated with the presence of pentagons within the graphene lattice [27]. In addition, the C-C/C-H peak, commonly attributed to sp^3 hybridized hydrocarbons, also increases due to the overlap between the binding energy line of hydrocarbons and that of carbon sp^2 bonds with nitrogen.

The fitting of both spectra and of future spectra was carried out following the procedure outlined in Annex III.

Similar to graphene, N-doped graphene coatings were compared to the N-doped powder pressed onto an indium substrate to evaluate whether the deposition process modifies the free-standing powder characteristics. The XPS quantification revealed that this type

of N-doped graphene is still very inert, with only 1.5 % oxygen, while getting 3.5 % nitrogen. By comparing the TEY of the free-standing powder and the best result of the deposited N-doped graphene, it can be concluded that EPD manages to get very close to the value of the powder material, as shown in Figure 4.7. These results demonstrate the high suitability of EPD for preserving the characteristics of the original material.

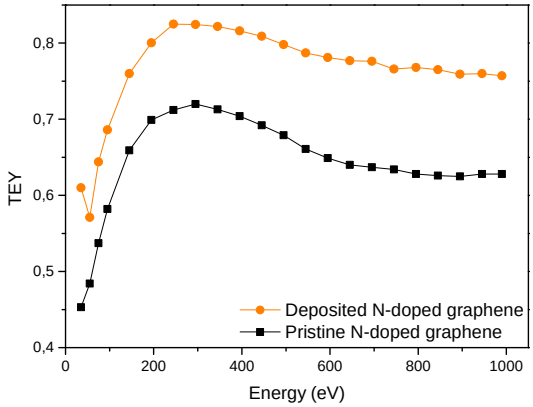

Figure 4.7: TEY as a function of the energy of the incident beam for Deposited N-doped graphene and Pristine N-doped graphene.

The maximum TEY obtained for the EPD deposited sample was 0.82±0.01, which is considerably lower than the requirement for the High Luminosity - Large Hadron Collider (HL-LHC), estimated at around 1.1. In that context, the designed cooling capacity is insufficient in high-load arcs, where a TEY of 1.35 has been reported, whereas in low-load arcs, a TEY of 1.25 was sufficient to withstand the beam intensity [52]. The large TEY margin enables further developments in the high-luminosity beam fields without compromising beam quality or the cooling system due to the electron cloud formation, while also allowing longer aging times before the TEY reaches values unsuitable for operation. The pristine N-doped graphene exhibited a maximum of 0.72±0.01. The first point of both curves can be disregarded, since at low energies the electron beam cross-section exceeds the sample area, generating secondary electrons from the metallic sample holder, which has a higher TEY.

The following two sub-chapters analyze the influence of the deposition parameters. In the case of N-doped graphene, an additional factor, temperature, was introduced and controlled using a thermal bath, since it was observed that the solution temperature increases with the applied voltage. For example, at 80 V over 101 minutes, the temperature rose from 26.0 °C to 27.6 °C, even with cooling at 16 °C. In contrast, when the same deposition was performed without cooling, the temperature increased from 32.5 °C to 55.7 °C within only 45 minutes. The shorter deposition time resulted from the complete consumption of graphene flakes in the solution, confirming that temperature strongly influences particle mobility and, consequently, the deposition rate.

4.2.1 Deposition Efficiency Analysis

In this work, TEY is used as the deposition response. However, since each factor combination was tested only once, the Taguchi Experimental Design could not be fully applied, as there were not enough repetitions to perform the variance analysis. Instead, the method was adapted to consider a single deposition per sample, i.e., instead of using the equations 2.13, one of the following equations is used to maximize the response for each factor [37]:

$$\xi = -10 \log \left(y^2 \right) \tag{4.1}$$

$$\xi = -10 \log \left(\frac{1}{y^2} \right) \tag{4.2}$$

where ξ is the maximized independent response and y is the system's response. The first equation was used when the considered parameter y should be minimized and the second when the parameter should be maximized.

The aim was not to eliminate the noise, but to filter out the contributions of other factors in order to isolate the effect of each parameter under study. This approach makes it possible to evaluate the relative influence of HCl concentration, applied voltage, and temperature on the system separately.

By following the steps described earlier, the average SN ratios for each factor were obtained:

The corresponding Δ values were 1.097, 0.448, and 0.889, respectively. Since $\Delta_c > \Delta_V > \Delta_T$, it can be concluded that HCl concentration is the most influential parameter during the deposition. This is evident in the graph 4.8(a), which reflects the balance between repulsive and attractive forces between particles that governs suspension stability. The presence of a clear local maximum indicates the optimal HCl concentration.

In contrast, both voltage and temperature exhibited smaller influences. While Δ_V is not far from Δ_c, making voltage still a relevant parameter, Δ_T was significantly smaller. However, temperature data are less reliable than those for HCl concentration and voltage, as several additional factors contributed: heat transfer through the electrodes due to the Joule effect, thermal losses between the hose and the beaker, temperature gradients inside the solution, and the increase in temperature caused by ultrasonication.

Further depositions covering a broader range of conditions would be necessary to refine the determination of the optimal responses for this system. Nevertheless, the results suggest that the optimal deposition parameters are approximately 80 μL of HCl in 37.5 mL of isopropanol, with a 20 V potential difference between the electrodes, and at either

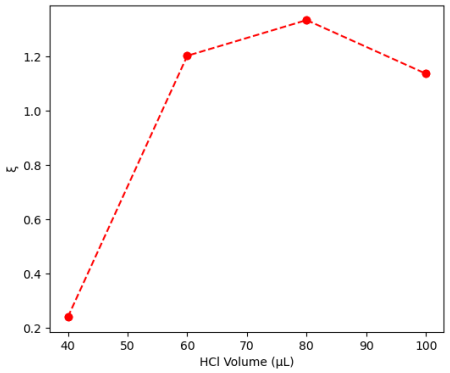

(a) HCl content.

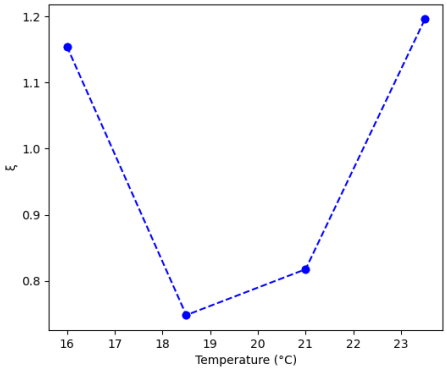

(b) Temperature.

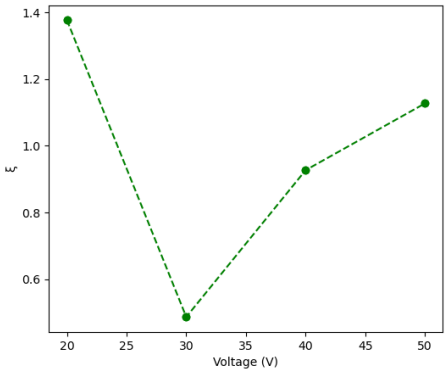

(c) Voltage.

Figure 4.8: Maximized independent response (TEY) as a function of deposition factors: (a) HCl Content (b) Temperature (c) Voltage.

low or high temperature. This conclusion is consistent with the best TEY value obtained in this work, recorded under the ideal HCl concentration and controlled temperature.

4.2.2 Chemical Composition Analysis

The same Taguchi-based approach can also be applied to other material characteristics of interest, such as the sp^2-to-sp^3 ratio, the pyrrolic-to-pyridinic ratio, and the nitrogen percentage.

For the sp^2/sp^3 ratio, the calculated Δ values were $\Delta_c = 1.459$, $\Delta_T = 2.914$, and $\Delta_V = 2.431$. These results indicate that temperature has the greatest influence on the preservation and contamination of the graphene powder. This effect may be related to the increased mobility of particles in the solution. At lower temperatures, deposition takes longer, increasing the likelihood of undesirable compounds adhering to the substrate, becoming trapped between the deposited layers, or remaining on the surface. At the same time, as the deposition process is slower, the graphene flakes have a wider time window to interact with the solution, which is a chemically active environment. Consequently, at higher temperatures, the sp^3 contribution is increased.

For the pyrrolic-to-pyridinic ratio, the Δ values were $\Delta_c = 1.972$, $\Delta_T = 1.576$, and $\Delta_V =$

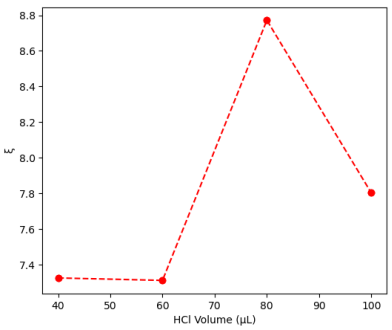

(a) HCl content.

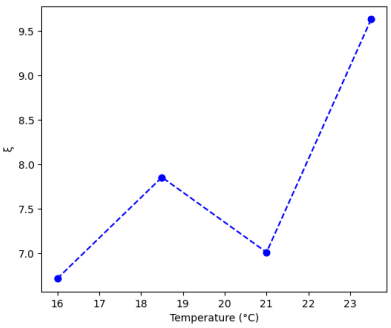

(b) Temperature.

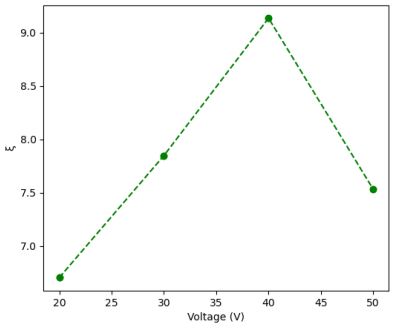

(c) Voltage.

Figure 4.9: Maximized independent response (sp^2/sp^3) as a function of deposition factors: (a) HCl Content (b) Temperature (c) Voltage

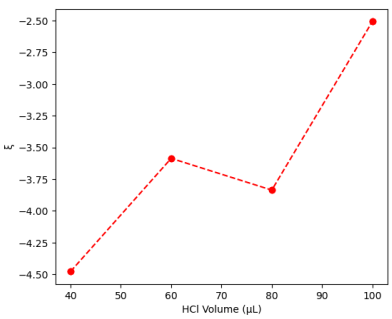

(a) HCl content.

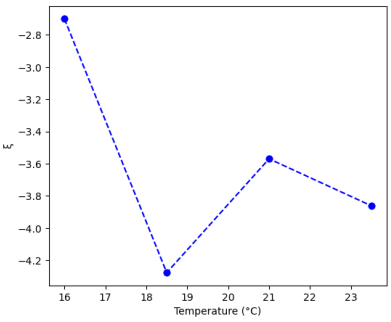

(b) Temperature.

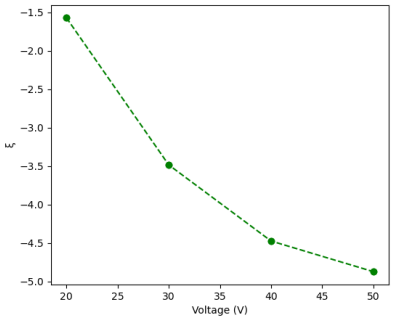

(c) Voltage.

Figure 4.10: Maximized independent response (pyrrolic-to-pyridinic ratio) as a function of deposition factors: (a) HCl Content (b) Temperature (c) Voltage.

3.303. In this case, a lower ratio is preferred, so the equation 4.2.1 is used to compute the average best response. Voltage is by far the most influential factor, with results showing an inverse relationship: higher voltages increase the proportion of pyrrolic bonds relative to pyridinic ones. Conversely, the ratio decreases with increasing HCl concentration, reaching a plateau in the 60–80 μL range.

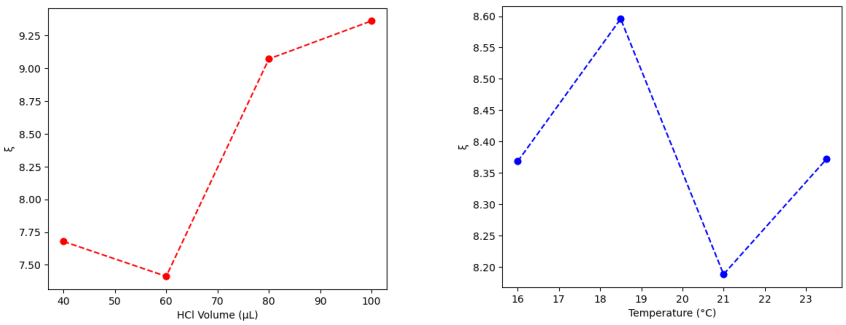

(a) HCl content.

(b) Temperature.

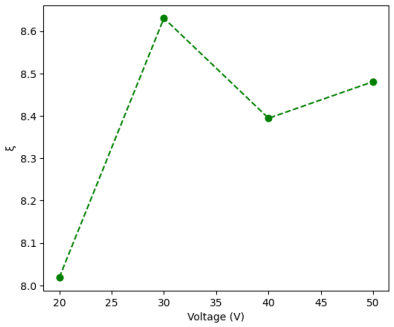

(c) Voltage.

Figure 4.11: Maximized independent response (N %) as a function of deposition factors: (a) HCl Content (b) Temperature (c) Voltage.

Finally, the nitrogen doping exhibited a strong dependence on HCl concentration, with Δ_c = 1.952, compared to Δ_T = 0.408 and Δ_V = 0.612. Since higher nitrogen incorporation is desirable, the equation 4.2.1 was used for the calculation. The importance of HCl concentration can be explained by the chemical reactivity of nitrogen with HCl. As reported in [53], HCl can play a role in nitrogen and boron doping of graphene oxide during acetylene hydrochlorination. Although HCl dissociates in the solution, making this reaction unlikely here, the ions may instead charge the surface of nitrogen-rich particles, giving them preference in the deposition process. In addition, H^+ ions may bond with OH^-, thereby reducing oxygen contamination in the sample. This interpretation is supported by the comparison of average oxygen content across the different HCl concentrations:

From this set of samples, it is possible to evaluate potential correlations between the previously discussed chemical characteristics and TEY, the key material property in this work. To facilitate this analysis and improve the readability of the plots, the data were averaged for each identical deposition parameter, yielding the following results:

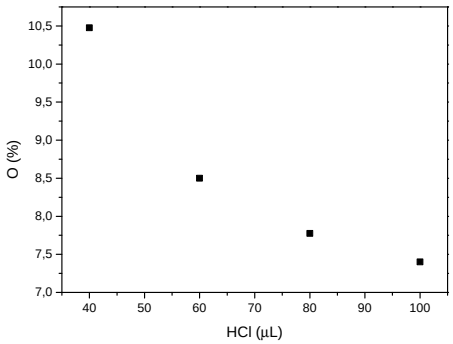

Figure 4.12: Oxygen content as a function of HCl concentration.

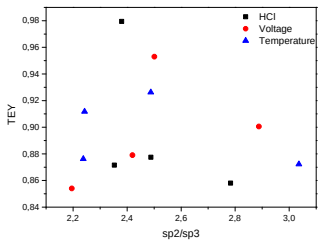

(a) sp^2-to-sp^3 ratio.

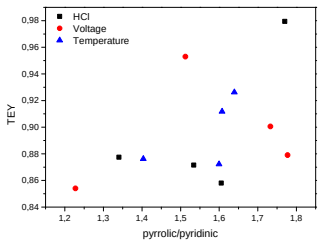

(b) pyrrolic-to-pyridinic ratio.

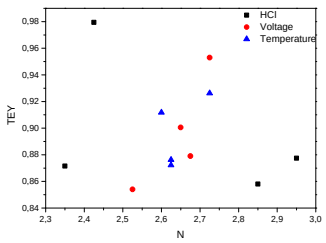

(c) N content.

Figure 4.13: TEY as a function of (a) sp^2-to-sp^3 ratio (b) pyrrolic-to-pyridinic ratio (c) N content.

At first glance, no definitive conclusions can be drawn directly from the trends. However, examining the dispersion of the data reveals two noteworthy observations. First, a wide spread of TEY values is observed at a low sp^2-to-sp^3 ratio in the Figure 4.13(a). As the ratio increases, the results become more confined, although the limited number of data points may partially account for this apparent trend. Second, in the case of the pyrrolic-to-pyridinic ratio (Graph 4.13(b)), the absence of pyrrolic bonds appears to consistently correlate with lower TEY. Nevertheless, this observation should be treated cautiously, as the available data remain insufficient to fundament a firm conclusion.

4.2.3 Raw Response Analysis

While the previous analysis isolated each factor using a Taguchi-based approach, it did not account for interactions between the parameters. To complement that method, conclusions were also drawn directly from the raw data, where only one deposition parameter was varied at a time while keeping the others fixed. The baseline conditions were 40 V, 60 μL of HCl, and 16 °C with controlled temperature for 97 minutes.

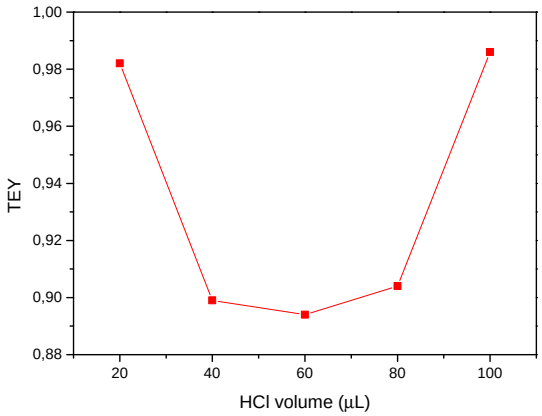

Figure 4.14: TEY as a function of HCl Content.

For these conditions, the optimal HCl volume in 37.5 mL of isopropanol was 60 μL, since this value produced the lowest maximum TEY among the samples, as can be seen in Figure 4.14.

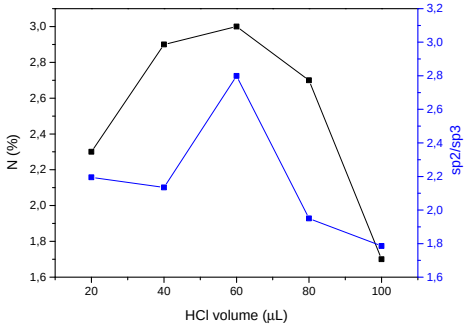

(a) Effect of HCl content on Nitrogen content and sp^2-to-sp^3 ratio.

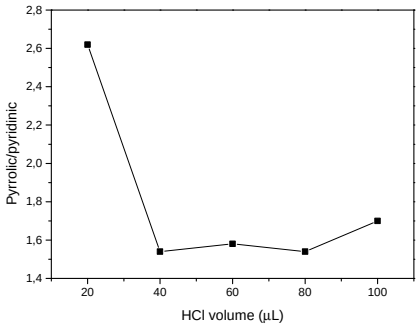

(b) Pyrrolic-to-pyridinic ratio as a function of HCl content.

Figure 4.15: Chemical composition dependence on HCl content.

A comparison of the doping percentage and sp^2-to-sp^3 ratio reveals that both peak at 60 μL, decrease as the concentration deviates from this value. This suggests that HCl volume plays a role in the intrinsic integrity of the graphene powder, as it can be seen in the annex VI.1, also affecting the cleanliness of the deposition, as sp^3 contributions mainly

originate from hydrocarbon contamination at the surface. Additionally, both characteristics correlate well with the TEY, as the higher they are, the lower the TEY, indicating that the preservation of the N-doped graphene powder is crucial for achieving the lowest maximum TEY, or one that is as close as possible to that of the pristine form. The pyrrolic-to-pyridinic ratio follows a similar trend to TEY, implying a correlation between them: lower ratios correspond to lower TEY values. Possible explanations include the presence of hydrogen in pyrrolic bonds, reported to reduce TEY in amorphous carbon [54], and different contributions to plasmon losses.

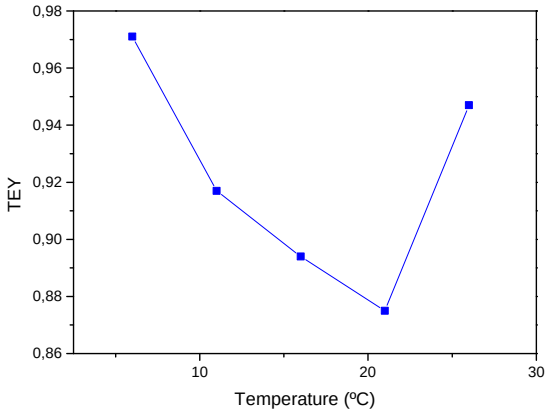

Figure 4.16: TEY as a function of temperature.

For temperature, a clear minimum is observed in the Figure 4.16 at 21 °C under controlled conditions. However, a definitive conclusion cannot be drawn, as the actual solution temperature fluctuates with time and external factors.

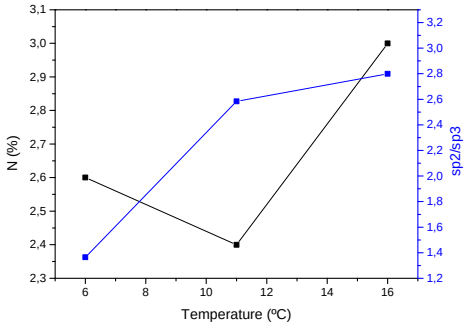

(a) Effect of the temperature on Nitrogen content and sp^2-to-sp^3 ratio.

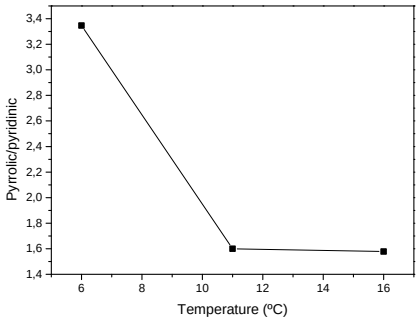

(b) Pyrrolic-to-pyridinic ratio as a function of temperature.

Figure 4.17: Chemical composition dependence on temperature control.

Temperature has a strong influence on particle mobility, which in turn affects coating quality and suspension stability. Different temperature ranges may select graphene sheets with different doping levels by the balance between the particles' aggregation and

their mobility. Higher temperatures appear to discourage hydrocarbon adsorption on the surface, which leads to lower TEY values, as can be seen in graph 4.16 for temperatures between 6 °C and 16 °C. As with HCl concentration, the pyrrolic-to-pyridinic ratio varies in the same way as TEY with temperature.

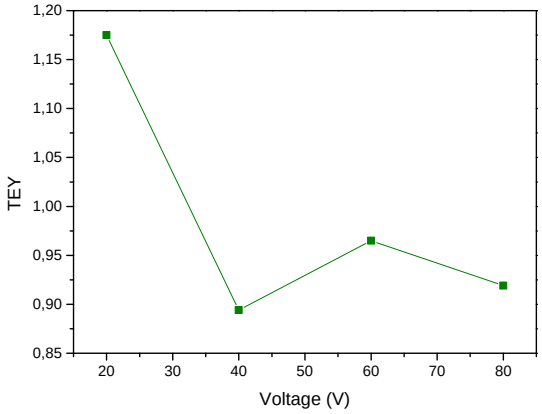

Figure 4.18: TEY as a function of voltage.

For voltage, very high TEY values were recorded at low voltages. Compared with the Taguchi dataset 4.8(c), the best-performing samples appeared at 20 V. However, this discrepancy is likely due to the presence of a large low-energy peak overlapping with the expected TEY maximum, making that point unreliable (Annex V).

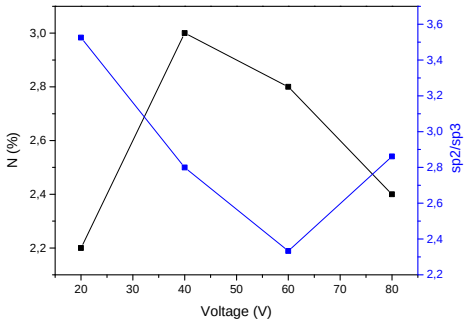

(a) Effect of the voltage on Nitrogen content and sp^2-to-sp^3 ratio.

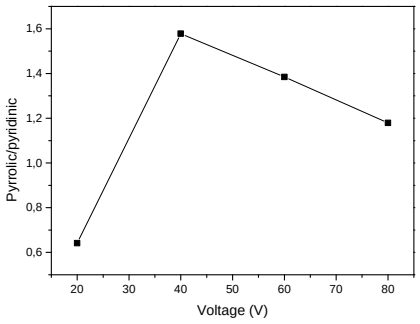

(b) Pyrrolic-to-pyridinic ratio as a function of voltage.

Figure 4.19: Chemical composition dependence on applied voltage.

Excluding the first data point, the results show that voltage significantly influences deposition quality. As reported in [33], voltage affects surface morphology, which in turn modifies the extent of surface contamination. At low voltages, graphene sheets tend to deposit parallel to the substrate, whereas at higher voltages they align more perpendicularly. This orientation difference can compromise the nitrogen percentage by reducing nitrogen retention at higher voltages. By examining the SEM images, presented in VI.2,

no clear orientation can be visualized. Although it is clearer that for lower magnitude images (VI.3), the surface morphology is indeed influenced by the applied voltage. The pyrrolic-to-pyridinic ratio decreases linearly with increasing voltage and, contrary to the other two previous parameters, this ratio has a different trend than the TEY.

Finally, it should be noted that the sp^2-to-sp^3 and pyrrolic-to-pyridinic ratios were obtained by fitting the C 1s and N 1s lines, respectively. As explained in Annex III, the fitting models influence the extracted values, which may differ from those reported in the literature when applied to the same spectra.

4.3 Graphene vs N-doped graphene

This section compares samples made using graphene and N-doped graphene in order to evaluate the efficiency of the EPD technique for each material. Since deposition parameters strongly influence sample characteristics, comparisons are restricted to the samples prepared under equivalent experimental conditions. However, it is important to note that exact equivalence was not possible: temperature control was only implemented during the deposition of N-doped graphene. Thus, comparisons are made on the basis of identical HCl concentrations and applied voltage. The latter is the same, 40 V, for all the samples.

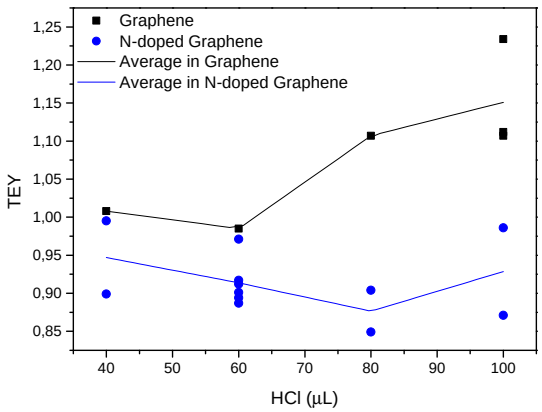

Figure 4.20: TEY as a function of HCl concentration for Graphene and N-doped graphene.

For low HCl concentrations, as can be seen in the Figure 4.20, the difference between graphene and N-doped graphene is practically the same, indicating that the EPD process proceeds similarly for both materials under these conditions. That difference can be attributed to the inherent characteristics of the powders, where the doped one presents lower TEY. At higher HCl concentrations, however, the gap widens, suggesting that N-doped graphene is inherently more suitable for EPD than its undoped counterpart.

The sp^2-to-sp^3 ratio exhibits a different behavior. In the case of N-doped graphene, this average ratio remains nearly constant across all HCl concentrations, yet it correlates

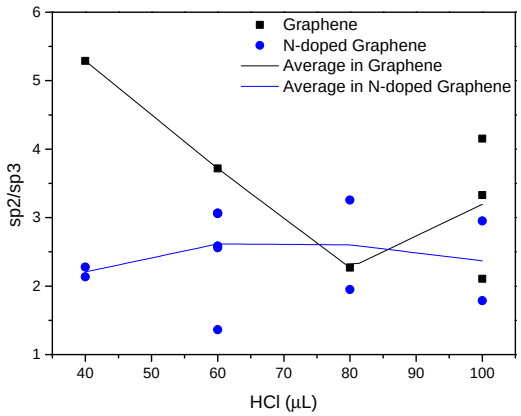

Figure 4.21: sp^2-to-sp^3 ratio as a function of HCl concentration for Graphene and N-doped graphene.

with TEY: higher sp^2 content corresponds to lower TEY values. Conversely, graphene shows no clear relationship between these two parameters. On average, EPD yields cleaner deposits when using graphene compared to N-doped graphene. A possible explanation is that N-doping increases activity and introduces additional dangling bonds, which facilitate the adsorption of hydrocarbons on the graphene lattice's edges and in the nitrogen pyrrolic sites.

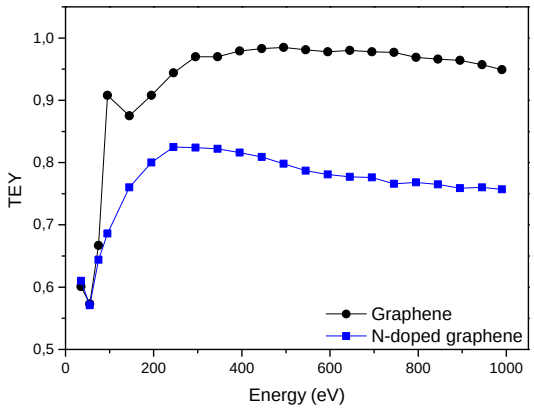

Figure 4.22: TEY as a function of the energy of the incident beam for Graphene and N-doped graphene.

When deposited by EPD, the differences become much more pronounced relative to the differences of TEY of the powders. The lowest maximum TEY achieved for EPD-deposited graphene was 0.98±0.01, representing an increase of 26 % of TEY when compared with the pristine powder. By contrast, for N-doped graphene, the maximum TEY was only 0.82±0.01, which converts to an increase of 14 % of the maximum TEY relative to the powder. This suggests that EPD preserves the intrinsic properties of N-doped

graphene more effectively, enhancing its performance relative to pristine graphene. Deposition conditions differed slightly: pristine graphene was deposited at 40 V with 60 μL HCl for 58 minutes, while N-doped graphene was deposited at 30 V with 80 μL HCl for 90 minutes, including a 45-minute break to redisperse the powder and improve suspension stability.

XPS analysis further confirms these differences. Unlike in the pristine powders, no visible π-plasmon loss is observed directly in the deposited spectra; however, line fitting shows a decrease from 3.31 % to 2.44 % after doping. The sp^2-to-sp^3 ratio also decreases from 3.72 in graphene to 3.20 in N-doped graphene, indicating higher hydrocarbon contamination in the latter. This is supported by oxygen quantification, which increases from 6,2 % in graphene to 10,0 % in N-doped graphene.

4.4 Additional Observations

In some cases, the nitrogen content quantified by XPS was lower than expected. One possible explanation is that surface hydrocarbons attenuated the photoelectrons emitted from bonds below the contamination layer. To test this hypothesis, a sample was annealed overnight at 100 °C. Before annealing, the sample contained 0.9 % nitrogen and 34.8 % oxygen. After the treatment, nitrogen remained nearly unchanged at 0.8 %, while oxygen increased to 37.8 %. Since the carbon content decreased as well, these results indicate that hydrocarbons evaporated during the annealing. Therefore, the low nitrogen level was not an artifact of contamination but rather reflected the intrinsic quality of the sample.

A second experiment was conducted to evaluate whether substrate position (facing the counter electrode or not) influenced the deposition. For this analysis, the sample originally used for TEY was characterized by XPS, while the one initially dedicated to XPS was subsequently measured by TEY.

Samples	TEY	C %	O %	N %	sp^2/sp^3	pyrrol/pyridin
1	0.89	90.2	7.2	2.6	3.07	1.58
2	0.89	89.5	7.0	3.4	2.53	1.53

Table 4.1: TEY, carbon content, oxygen content, nitrogen content, sp^2-to-sp^3 ratio, and pyrrolic-to-pyridinic ratio for samples deposited in different orientations relative to the counter electrode.

As can be seen in Table 4.1, the first sample was positioned facing the counter electrode, whereas the second was mounted back-to-back with the first. Both measurements yielded similar electronic responses. However, a visible difference in deposition amount was observed. Sample 2 exhibited less material on its surface, consistent with its position in the cell. Facing a region of the solution where replenishment of suspended

graphene was more limited, this sample experienced a reduced powder concentration over the course of deposition, leading to a thinner coating.

5

Conclusion and Future Prospects

The main objective of this work was to assess the feasibility of using EPD as a technique to produce N-doped graphene coatings from free-standing N-doped graphene powder while preserving its initial properties. This approach aims to further reduce the TEY in various technological applications, such as particle accelerators and different Radio Frequency (RF) devices, by coating copper substrates, to represent the material typically used in these systems.

Achieving the proposed goals required optimization of the EPD parameters to minimize TEY, using isopropanol as the solvent and HCl as the electrolyte. Initially, the applied voltage and HCl concentration were the only deposition factors, followed by temperature control for N-doped graphene. For each sample, TEY measurements were complemented by XPS surface analysis, enabling a comprehensive evaluation of the deposited coatings.

The most significant outcome of this study was the achievement of an exceptionally low TEY of 0.82, along with numerous results below 0.9, substantially lower than the TEY requirement at the LHC, which is approximately 1.3. This result secures the margin for the aging.

To familiarize with the EPD technique and validate previous findings, initial depositions were carried out using undoped graphene. XPS analysis and TEY measurement revealed a clear correlation between TEY and sp^2-to-sp^3 ratio: the higher the ratio, the lower the TEY. This observation aligns with literature reports indicating that sp^3 hybridization enhances SEE. In this work, the sp^3 content primarily originated from hydrocarbon adsorption on graphene sheets. Additionally, higher HCl concentrations were found to increase TEY, as they can promote degradation of the carbon lattice and enhance hydrocarbon and oxygen contamination. Oxygen, however, does not appear to negatively affect TEY.

Nitrogen doping modifies graphene's electronic structure, leading to changes in TEY due to the loss of a free π electron, as well as the reduction of π-plasmons. Defects introduced during the doping can also influence secondary electron emission. These effects

were confirmed by comparing the XPS spectra of undoped and N-doped graphene powders.

For the deposition, an additional factor, not initially considered, was found to play a crucial role in controlling TEY, oxygen contamination, and deposition time: the temperature. At higher temperatures inside the solution, up to 16 °C, particle mobility increases, improving deposition efficiency, while also reducing hydrocarbon adsorption.

By adapting Taguchi's method to the experimental conditions, it was possible to identify the influence of each deposition parameter on the sample's characteristics independently. HCl concentration emerged as the most critical factor, strongly affecting TEY nitrogen content, N-doped graphene powder integrity, and surface cleanliness. Temperature control was crucial in minimizing hydrocarbon contamination and enhancing suspension stability, while the applied voltage primarily affected the pyrrolic-to-pyridinic ratio. This led to the conclusion that the optimal deposition conditions for N-doped graphene were determined to be 80 μL HCl in 37.5 mL isopropyl alcohol, 20 V applied voltage, and a temperature control, by a thermal bath, of 23 °C.

As with undoped graphene, N-doped graphene exhibited the same TEY dependence on sp^2-to-sp^3 ratio. However, N-doped graphene showed higher contamination levels due to the larger number of dangling bonds associated with defects and pyrrolic bonding, which facilitate sp^3 adsorption. In contrast, N-doped graphene better preserved its initial powder properties and consistently achieved lower TEY values, demonstrating its greater suitability for EPD applications.

Nevertheless, further investigations are necessary to fully elucidate the role of each deposition parameter. One important improvement would be to measure the actual solution temperature, and possibly stabilize it, to strengthen the conclusions regarding the thermal effects. Additionally, further surface topography analysis would provide valuable insights into the actual structure of the deposited coating and thickness measurement, along with Raman spectroscopy of the samples deposited by EPD to evaluate if those nanoparticles are made from graphene. Moreover, exploring alternative methods to enhance coating adhesion, such as copper surface functionalization or the use of intermediate thin films, would also be beneficial. As the XPS is used to analyze the electronic structure of the core levels of a surface, employing Ultraviolet Photoelectron Spectroscopy (UPS) to study the valence band structure, together with work function measurements, could further deepen the understanding of the underlying physical mechanisms governing TEY reduction in these coatings.

Bibliography

[1] J. M. Lourenço. *The NOVAthesis LaTeX Template User's Manual*. NOVA University Lisbon. 2021. URL: https://github.com/joaomlourenco/novathesis/raw/main/template.pdf (cit. on p. i).

[2] P. C. Pinto et al. "Carbon coatings with low secondary electron yield". In: *Vacuum* 98 (2013), pp. 29–36. ISSN: 0042207X. DOI: 10.1016/j.vacuum.2013.03.001 (cit. on pp. 1, 2).

[3] R. Aguincha et al. "Low total electron yield graphene coatings produced by electrophoretic deposition". In: *Applied Surface Science* 504 (2020-02). ISSN: 01694332. DOI: 10.1016/j.apsusc.2019.143870 (cit. on pp. 1, 6, 32).

[4] P. Kumar et al. "The dose effect in secondary electron emission". In: *IEEE Transactions on Plasma Science* 37 (8 PART 2 2009), pp. 1537–1551. ISSN: 00933813. DOI: 10.1109/TPS.2009.2022970 (cit. on pp. 1, 4).

[5] J. J. Nivas et al. "Secondary electron yield reduction by femtosecond pulse laser-induced periodic surface structuring". In: *Surfaces and Interfaces* 25 (2021-08). ISSN: 24680230. DOI: 10.1016/j.surfin.2021.101179 (cit. on pp. 1, 3, 4, 9).

[6] V. Baglin et al. "THE SECONDARY ELECTRON YIELD OF TECHNICAL MATERIALS AND ITS VARIATION WITH SURFACE TREATMENTS". In: *7th European Particle Accelerator Conference*. Ed. by W. A. Mitaroff et al. CERN, 2000-09, pp. 217–221. URL: https://cds.cern.ch/record/466534/files/lhc-project-report-433.pdf (cit. on pp. 1, 4).

[7] K. Harkay. "Electron cloud observations: a retrospective". In: (2005) (cit. on pp. 1, 2).

[8] F. Zimmermann and G. Switzerland. "ELECTRON CLOUD EFFECTS IN ACCELERATORS". In: *ECLOUD'18: Proceedings of the Joint INFN-CERN-ARIES Workshop on Electron-Cloud Effects*. Ed. by R. Cimino, G. Rumolo, and F. Zimmermann. CERN Yellow Reports: Conference Proceedings, 2018-06, pp. 1–8. DOI: 10.48550/arXiv.1310.1706 (cit. on p. 2).

[9] A. R. and G. Switzerland. "SEY AND ELECTRON CLOUD BUILD-UP WITH NEG MATERIALS". In: *ECLOUD'04 : 31st Advanced ICFA Beam Dynamics Workshop on Electron-Cloud Effects*. Ed. by M. Furman, S. Henderson, and F. Zimmermann. CERN, 2005-01, pp. 113–117. DOI: 10.5170/CERN-2005-001.113 (cit. on p. 3).

[10] I. Montero et al. "Secondary electron emission under electron bombardment from graphene nanoplatelets". In: *Applied Surface Science* 291 (2014-02), pp. 74–77. ISSN: 01694332. DOI: 10.1016/j.apsusc.2013.10.045 (cit. on p. 3).

[11] R. Miguel and S. Aguincha. "Carbon Based Surfaces with Low Secondary Electron Emission". PhD thesis. Faculdade de Ciências e Tecnologia da Universidade Nova de Lisboa, 2018-09. URL: http://hdl.handle.net/10362/56374 (cit. on p. 3).

[12] J. B. Wang et al. "A review of graphene synthesis at low temperatures by CVD methods". In: *Xinxing Tan Cailiao/New Carbon Materials* 35 (3 2020-05), pp. 193–208. ISSN: 18725805. DOI: 10.1016/S1872-5805(20)60484-X (cit. on p. 3).

[13] M. Peng et al. "Effect of the Surface Morphology of Porous Coatings on Secondary Electron Yield of Metal Surface". In: *Materials* 15 (12 2022-06). ISSN: 19961944. DOI: 10.3390/ma15124322 (cit. on p. 4).

[14] N. Bundaleska et al. "Prospects for microwave plasma synthesized N-graphene in secondary electron emission mitigation applications". In: *Scientific Reports* 10 (1 2020-12). ISSN: 20452322. DOI: 10.1038/s41598-020-69844-9 (cit. on pp. 4, 12, 56, 61).

[15] M. Chodorow et al. "16 - Electron Tubes". In: ed. by W. M. Middleton and M. E. V. Valkenburg. 9th ed., pp. 1–59. ISBN: 9780750672917. DOI: 10.1016/B978-075067291-7/50018-2 (cit. on p. 5).

[16] JEOL. *reflected electron, backscattered electron*. https://www.jeol.com/words/semterms/20121024.0728 pgsc.tab=0 (cit. on p. 5).

[17] A. Shih et al. "Secondary electron emission studies". In: *Applied Surface Science*. Vol. 111. 1997, pp. 251–258. DOI: 10.1016/S0169-4332(96)00729-5 (cit. on p. 5).

[18] B.-J. Á. Shaw. "Shaw$_2$010". PhD thesis. FCT/UNL, 2010-10 (cit. on pp. 6, 28).

[19] M. P. Seah and W. A. Dench. "Quantitative electron spectroscopy of surfaces: A standard data base for electron inelastic mean free paths in solids". In: *Surface and Interface Analysis* 1.1 (1979), pp. 2–11. DOI: https://doi.org/10.1002/sia.740010103. eprint: https://analyticalsciencejournals.onlinelibrary.wiley.com/doi/pdf/10.1002/sia.740010103. URL: https://analyticalsciencejournals.onlinelibrary.wiley.com/doi/abs/10.1002/sia.740010103 (cit. on p. 8).

[20] R. Egerton. *Electron Energy-Loss Spectroscopy in the Electron Microscope*. Springer US, 2011. DOI: 10.1007/978-1-4419-9583-4 (cit. on p. 8).

[21] M. Ye, D. Wang, and Y. He. "Mechanism of total electron emission yield reduction using a micro-porous surface". In: *Journal of Applied Physics* 121 (12 2017-03). ISSN: 10897550. DOI: 10.1063/1.4978760 (cit. on p. 9).

[22] W. Z. Cui et al. "An efficient multipaction suppression method in microwave components for space application". In: *Chinese Physics B* 25 (6 2016-06). ISSN: 20583834. DOI: 10.1088/1674-1056/25/6/068401 (cit. on p. 9).

[23] N. Bundaleski et al. "Calculation of the angular dependence of the total electron yield". In: *Vacuum* 122 (2015-12), pp. 255–259. ISSN: 0042207X. DOI: 10.1016/j.vacuum.2015.04.010 (cit. on p. 9).

[24] F. Schäffel. "The Atomic Structure of Graphene and Its Few-layer Counterparts". In: *Graphene: Fundamentals and emergent applications*. Elsevier, 2012-12, pp. 5–59. ISBN: 9780123948274. DOI: 10.1016/B978-0-12-394593-8.00002-3 (cit. on p. 10).

[25] C. S. Allen, J. H. Warner, and M. H. Rümmeli. "Properties of Graphene". In: *Graphene: Fundamentals and emergent applications*. Elsevier, 2012-12, pp. 61–127. ISBN: 9780123948274. DOI: 10.1016/B978-0-12-394593-8.00003-5 (cit. on pp. 11, 12).

[26] A. G. Marinopoulos et al. "Ab initio study of the optical absorption and wave-vector-dependent dielectric response of graphite". In: *Physical Review B - Condensed Matter and Materials Physics* 69 (24 2004). ISSN: 01631829. DOI: 10.1103/PhysRevB.69.245419 (cit. on p. 11).

[27] M. Ayiania et al. "Deconvoluting the XPS spectra for nitrogen-doped chars: An analysis from first principles". In: *Carbon* 162 (2020-06), pp. 528–544. ISSN: 00086223. DOI: 10.1016/j.carbon.2020.02.065 (cit. on pp. 12, 13, 34, 65, 66).

[28] T. Kato et al. "Origins of peaks of graphitic and pyrrolic nitrogen in N1s X-ray photoelectron spectra of carbon materials: quaternary nitrogen, tertiary amine, or secondary amine?" In: *Journal of Materials Science* 56 (28 2021-10), pp. 15798–15811. ISSN: 15734803. DOI: 10.1007/s10853-021-06283-5 (cit. on p. 13).

[29] M. Li et al. "An overview of graphene-based hydroxyapatite composites for orthopedic applications". In: *Bioactive Materials* 3 (1 2018-03), pp. 1–18. ISSN: 2452199X. DOI: 10.1016/j.bioactmat.2018.01.001 (cit. on p. 14).

[30] J. J. V. Tassel and C. A. Randall. "Mechanisms of Electrophoretic Deposition". In: *Key Engineering Materials* 314 (2006-07), pp. 167–174. DOI: 10.4028/www.scientific.net/kem.314.167 (cit. on p. 14).

[31] P. Westbroek. "Fundamentals of electrochemistry". In: *Analytical Electrochemistry in Textiles*. Woodhead Publishing, 2005-01, pp. 3–36. ISBN: 978-1-85573-919-2. DOI: 10.1533/9781845690878.1.1 (cit. on p. 14).

[32] Analytik. *Zeta Potential – What is it and how can it be characterised?* https://analytik.co.uk/zeta-potential-what-is-it-and-how-can-it-be-characterised/ (cit. on p. 15).

[33] L. Besra and M. Liu. "A review on fundamentals and applications of electrophoretic deposition (EPD)". In: *Progress in Materials Science* 52 (1 2007-01), pp. 1–61. ISSN: 00796425. DOI: 10.1016/j.pmatsci.2006.07.001 (cit. on pp. 15–17, 43).

[34] N. Koura et al. "Preparation of Various Oxide Films by an Electrophoretic Deposition Method: A Study of the Mechanism". In: *Jpn. J. Appl. Phys.* (1995), pp. 1643–1647. DOI: 10.1143/JJAP.34.1643 (cit. on p. 16).

[35] R. N. Basu, C. A. Randall, and M. J. Mayo. "Fabrication of Dense Zirconia Electrolyte Films for Tubular Solid Oxide Fuel Cells by Electrophoretic Deposition". In: *Journal of the American Ceramic Society* 84 (1 2001), pp. 33–40. ISSN: 00027820. DOI: 10.1111/j.1151-2916.2001.tb00604.x (cit. on p. 17).

[36] A. Rogacs and J. G. Santiago. "Temperature effects on electrophoresis". In: *Analytical Chemistry* 85 (10 2013-05), pp. 5103–5113. ISSN: 00032700. DOI: 10.1021/ac400447k (cit. on p. 18).

[37] I. N. Vuchkov and L. N. Boyadjieva. *Quality Improvement with Design of Experiments*. Ed. by A. Z. Keller. 1st ed. Springer Dordrecht, 2001. DOI: 10.1007/978-94-009-0009-7 (cit. on pp. 18, 36).

[38] D. N. G. Krishna and J. Philip. "Review on surface-characterization applications of X-ray photoelectron spectroscopy (XPS): Recent developments and challenges". In: *Applied Surface Science Advances* 12 (2022-12). ISSN: 26665239. DOI: 10.1016/j.apsadv.2022.100332 (cit. on p. 19).

[39] P. A. Schultz and R. P. Messmer. "SHIFT IN XI'S LEVELS IN IONIC ADSORBATE LAYERS DUE TO ELECTROSTATIC EFFECTS". In: *Surface Science*. Vol. 209. 1989, pp. 229–242. DOI: 10.1016/0039-6028(89)90070-8 (cit. on p. 19).

[40] S. Koxixi, K. Oxi, and F. Konisxt. "Extra-Atomic Relaxation Effect on the Binding Energy Reference Gold in X-Ray Photoelectron Spectroscopy". In: *ANALYTICAL SCIENCES* 1 (1985), p. 115. DOI: 10.2116/analsci.1.115 (cit. on p. 19).

[41] K. Oura et al. *Surface Science-An Introduction*. Springer, 2003. DOI: 10.1007/978-3-662-05179-5 (cit. on pp. 20, 21).

[42] J. F. Moulder et al. *Handbook of X-ray Photoelectron Spectroscopy A Reference Book of Standard Spectra for Identification and Interpretation of XPS Data*. Ed. by J. Chastain. Physical Electronics Division, Perkin-Elmer Corporation, 1979. ISBN: 0962702625,9780962702624 (cit. on pp. 20, 29).

[43] M. B. (UWO). *Multiplet Splitting*. https://xpslibrary.com/multiplet-splitting-2/. 2009 (cit. on p. 21).

[44] A. R. G. E. Pires. "INFLUENCE OF NITROGEN DOPING OF AMORPHOUS CARBON ON ITS SECONDARY ELECTRON YIELD". PhD thesis. NOVA School of Science and Technology, 2024-09. URL: http://hdl.handle.net/10362/182315 (cit. on p. 21).

[45] R. University. *X-ray Photoelectron Spectroscopy (XPS)*. https://www.ru.ac.za/media/rhodesuniversity/content/nanotechnology/documents/XPS.pdf (cit. on p. 22).

[46] M. P. Seah. "Simple universal curve for the energy-dependent electron attenuation length for all materials". In: *Surface and Interface Analysis* 44 (10 2012), pp. 1353–1359. ISSN: 10969918. DOI: 10.1002/sia.5033 (cit. on p. 22).

[47] J. C. Vickerman and I. S. Gilmore, eds. *Surface Analysis-The Principal Techniques 2nd Edition*. 2nd ed. Wiley, 2009. ISBN: 978-0-470-01763-0. DOI: 10.1002/9780470721582 (cit. on p. 22).

[48] W. Zhou et al. "Fundamentals of Scanning Electron Microscopy". In: *Scanning Microscopy for Nanotechnology*. Ed. by W. Zhou and Z. L. Wang. Springer, New York, NY, 2007-03, pp. 1–40. ISBN: 978-0-387-39620-0. DOI: https://doi.org/10.1007/978-0-387-39620-0_1 (cit. on pp. 23, 24).

[49] Bruker. *What is EDS/EDX? Introducing Energy Dispersive X-Ray Spectroscopy*. https://www.bruker.com/en/landingpages/bna/technology/what-is-eds.html. 2025 (cit. on p. 24).

[50] N. H. Turner and J. A. Schreifels. "Surface Analysis: X-ray Photoelectron Spectroscopy and Auger Electron Spectroscopy". In: *Analytical Chemistry*. Vol. 68. American Chemical Society, 1996, pp. 309–331. DOI: 10.1021/a19600146. URL: https://pubs.acs.org/sharingguidelines (cit. on p. 29).

[51] C. D. Wagner. *NIST x-ray photoelectron spectroscopy (XPS) database*. National Bureau of Standards, 1990. DOI: 10.6028/NIST.TN.1289. URL: https://nvlpubs.nist.gov/nistpubs/Legacy/TN/nbstechnicalnote1289.pdf (cit. on p. 31).

[52] G. Skripka and G. Iadarola. "Beam-induced heat loads on the beam screens of the HL-LHC arcs". In: (2019). URL: https://cds.cern.ch/record/2692753 (cit. on p. 35).

[53] B. Dai et al. "Boron and Nitrogen Doping in Graphene for the Catalysis of Acetylene Hydrochlorination". In: *ACS Catalysis* 5 (4 2015-04), pp. 2541–2547. ISSN: 21555435. DOI: 10.1021/acscatal.5b00199 (cit. on p. 39).

[54] C. F. Adame. "DEPARTMENT OF PHYSICS INFLUENCE OF HYDROGEN CONTAMINATION ON ELECTRON EMISSION PROPERTIES OF AMORPHOUS CARBON COATINGS USED IN PARTICLE ACCELERATORS". PhD thesis. NOVA School of Science and Technology, 2021-11. URL: http://hdl.handle.net/10362/140861 (cit. on p. 42).

[55] F. Fabry, G. Flamant, and L. Fulcheri. "Carbon black processing by thermal plasma. Analysis of the particle formation mechanism". In: *Chemical Engineering Science* 56.6 (2001), pp. 2123–2132. ISSN: 0009-2509. DOI: https://doi.org/10.1016/S0009-2509(00)00486-3. URL: https://www.sciencedirect.com/science/article/pii/S0009250900004863 (cit. on p. 59).

[56] W. Wei et al. "Predicting chemical emissions from household cleaning and personal care products: A review". In: *Building and Environment* 207 (2022-01). ISSN: 03601323. DOI: 10.1016/j.buildenv.2021.108483 (cit. on p. 62).

[57] W. M. Meylan and P. H. Howard. "Estimating octanol-air partition coefficients with octanol-water partition coefficients and Henry's law constants". In: *Chemosphere* 61 (5 2005), pp. 640–644. ISSN: 00456535. DOI: 10.1016/j.chemosphere.2005.03.029 (cit. on p. 62).

[58] M. C. Biesinger. "Advanced analysis of copper X-ray photoelectron spectra". In: *Surface and Interface Analysis* 49 (13 2017-12), pp. 1325–1334. ISSN: 10969918. DOI: 10.1002/sia.6239 (cit. on pp. 63, 64).

[59] J. D. Henderson et al. "Enhancing Oxygen Spectra Interpretation by Calculating Oxygen Linked to Adventitious Carbon". In: *Surface and Interface Analysis* 57 (3 2025-03), pp. 214–220. ISSN: 10969918. DOI: 10.1002/sia.7376 (cit. on p. 64).

[60] M. C. Biesinger. "Accessing the robustness of adventitious carbon for charge referencing (correction) purposes in XPS analysis: Insights from a multi-user facility data review". In: *Applied Surface Science* 597 (2022-09). ISSN: 01694332. DOI: 10.1016/j.apsusc.2022.153681 (cit. on p. 66).

A

Further analysis of the materials

An additional analysis of the deposited materials is presented, along with their surface morphology comparison with that of the pristine.

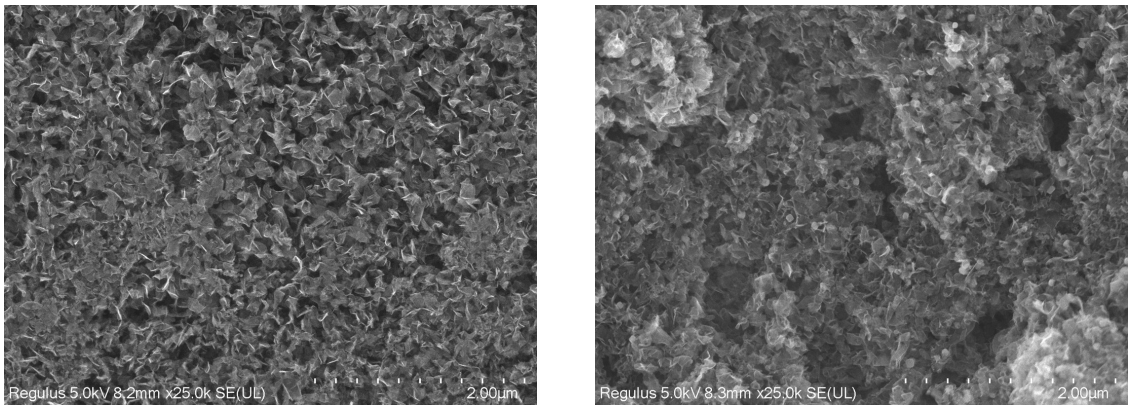

(a) Pristine Graphene. (b) Deposited Graphene.

Figure A.1: SEM images of (a) Pristine Graphene and (b) Deposited Graphene.

In both images in the Figure A.1, graphene can be observed in sheet-like structures, which is a good indicator of actual graphene deposition. In the second image, there is evidence of additional structures. Since this SEM image corresponds to the deposited sample, those structures may arise from the contamination within the sample, as both sp_3 and oxygen content increase in this type of sample, as described in Section 4.1. To support this conclusion, Raman spectroscopy was performed on both samples.

The spectra in the Figure A.2 present the three main characteristic graphene peaks: G, D, and 2D. By comparing them with previous studies of graphene [14], it is clear that the deposited material is undoubtedly graphene. The very high intensity of the 2D/G ratio in both spectra is the proof of a few-layer graphene in both samples.

Regarding the N-doped carbon material, the same procedure was carried out to determine whether the nanoparticle formation resulted from the EPD process or if the material inherently possessed such morphology.

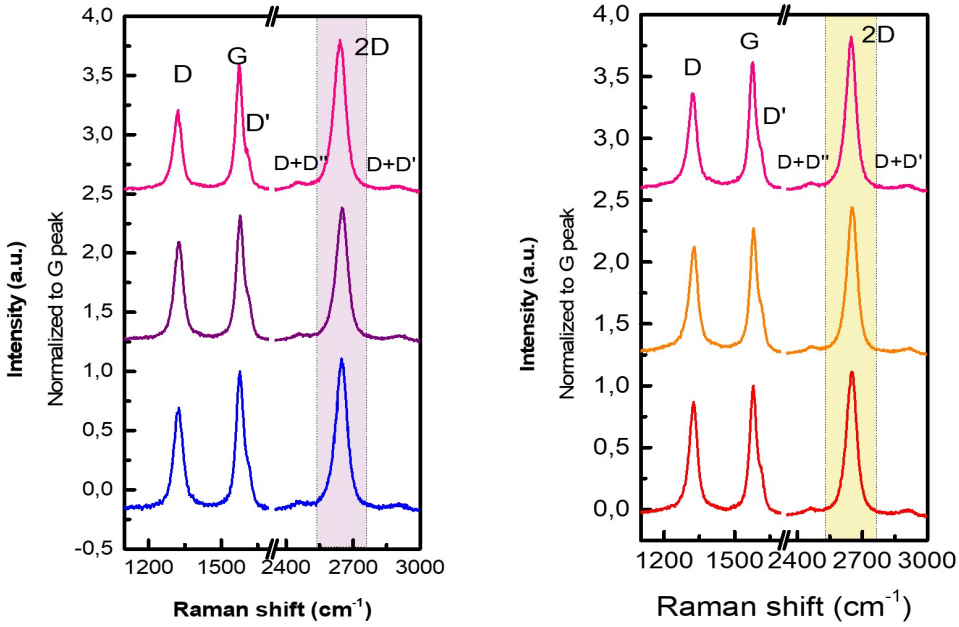

(a) Pristine Graphene.

(b) Deposited Graphene.

Figure A.2: Raman spectra of (a) Pristine Graphene and (b) Deposited Graphene.

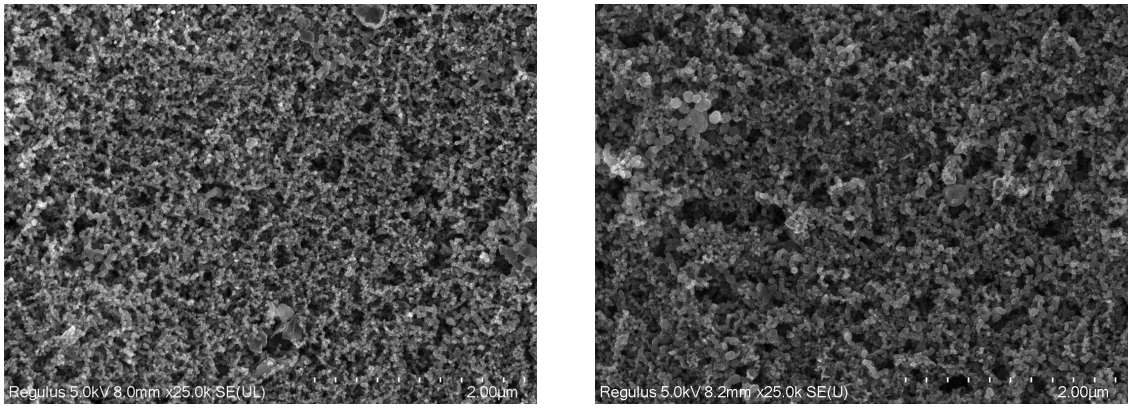

(a) Pristine Graphene.

(b) Deposited Graphene.

Figure A.3: Surface SEM images of (a) Pristine N-doped Graphene and (b) Deposited N-doped Graphene.

By examining the morphology of the pristine sample in the Figure A.3 and the deposited sample in the Figure A.3(b), it is possible to confirm that the nanoparticles are formed during the material synthesis. As before, the Raman spectroscopy supports this conclusion, also showing that the two-phonon scattering process associated with the 2D band is less frequent compared with graphene, and that the D and G bands are broadened (Figure A.4).

Both the pristine and the deposited materials have the same morphology, showing that the material features were preserved, although being different from the ones presented in Figure A.1. It appears that the N-doped graphene samples contain numerous spherical nanoparticles of the typical size of 25-75 nm, which were formed during the material synthesis. The Raman spectroscopy analysis presented in Figure A.4 of the two samples confirms their similarity. While these Raman spectra are different from those of the pure graphene, the G, D, and 2D bands (being the fingerprints of graphene) can still be clearly identified. Broad G and D bands and relatively low intensity of the 2D band imply the defective character of the N-doped graphene.

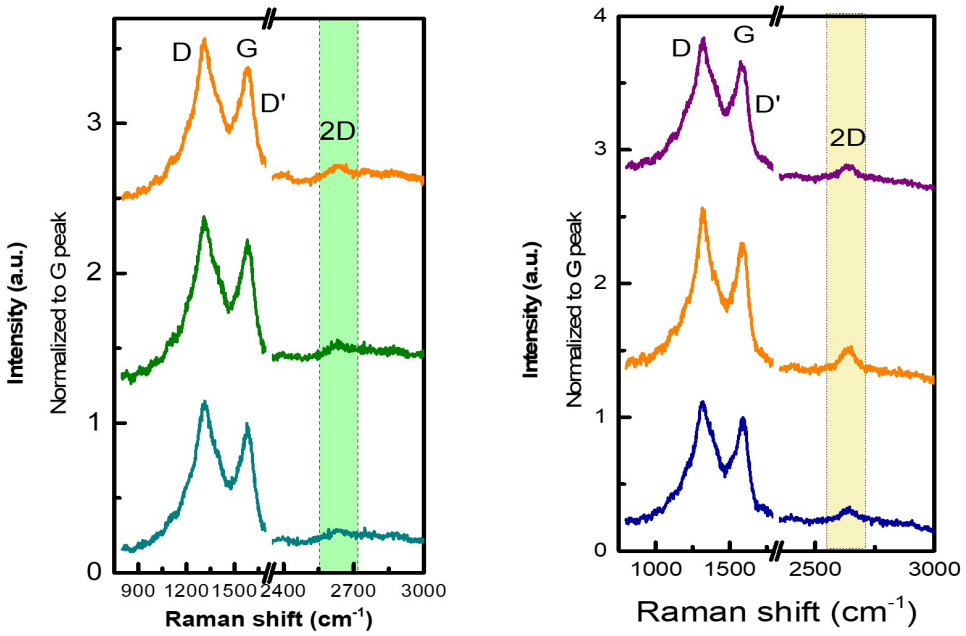

(a) Pristine N-doped Carbon Nanoparticles.

(b) Deposited N-doped Carbon Nanoparticles.

Figure A.4: Raman spectra of (a) Pristine N-doped Carbon Nanoparticles and (b)Deposited N-doped Carbon Nanoparticles.

This difference also explains why the sp_3 peak in the C 1s line, after excluding the doping contribution, increases in this type of material. As shown in the Figure 4.6, the sp_3 carbon content is only 4.5 % in pristine graphene, while in the N-doped carbon nanoparticles it reaches 37.1 %, once again indicating that they are distinct materials. A deeper study of these nanoparticles was performed using X-Ray Diffraction (XRD).

The spectrum in the Figure A.5 indicates an interlayer distance of 0.34 nm. This value

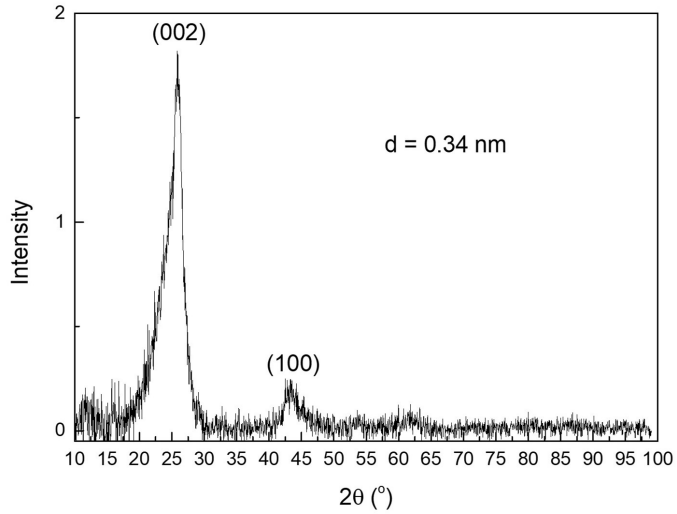

Figure A.5: XRD spectrum of the nanoparticles.

is very close to the one reported by [55] for the interlayer distance of graphite, 0.335 nm, indicating that the nanoparticles are graphitic structures. However, further study is required to better understand the material.

Moreover, the thickness of this material after deposition was measured by analysing SEM cross-section images.

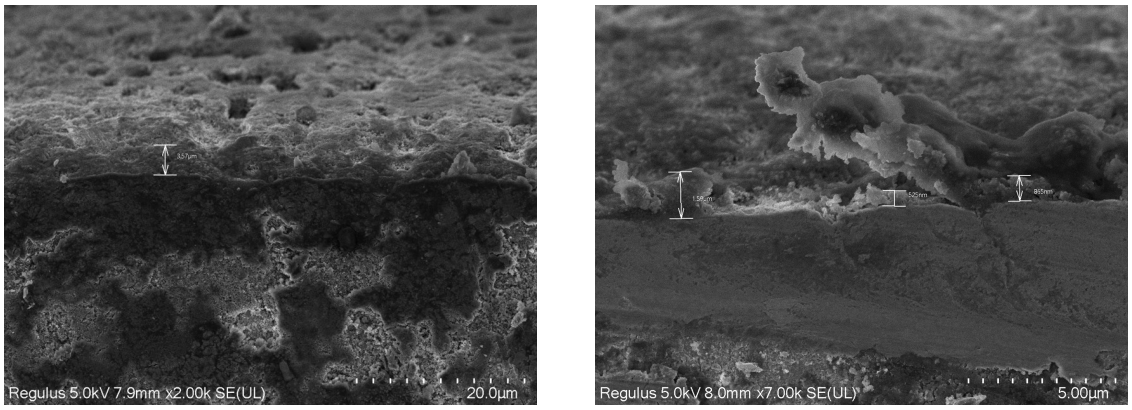

(a) Pristine N-doped Carbon Nanoparticles.

(b) Deposited N-doped Carbon Nanoparticles.

Figure A.6: Cross-section of different locations within the same deposited N-doped Carbon Nanoparticle sample.

As can be seen in the Figure A.6, the thickness varies from 500 nm to almost 4 μm. This variation occurs within the same sample, as the deposition is not uniform, and, when compared with other samples, it depends on the deposition parameters.

I

Production of N-doped free-standing graphene powder

The nitrogen-doped graphene structures used in the present study were synthesized by direct microwave plasma (2.45 GHz) method at atmospheric pressure. The method is based on the introduction of a carbon/nitrogen precursor (acetonitrile) into a microwave argon plasma environment, where decomposition of the precursor molecules via collisions and different chemical reactions takes place, and carbon atoms and molecules are created. The gas-phase species are then transported into the colder zone of the reactor, resulting in the transformation into solid carbon nuclei. The latter are gradually withdrawn with the outlet plasma stream, where kinetic energy processes of assembly and growth of "flowing" carbon nanostructures occur. Having in mind that nucleation and growth processes are determined by the interplay of kinetic and thermodynamic factors, the desired nanostructures synthesis is achieved via synergistic tailoring of the thermodynamic conditions of the different zones of the plasma reactor. Namely, by adjusting the temperature gradients, number density of carbon molecules and atoms as well as their residence time, selective synthesis of N-graphene sheets in a narrow range of operational parameters can be achieved. The assembled structures are in the form of free-standing N-graphene sheets, i.e., not attached to or grown on a substrate, as a light, fluffy powder.

Raman spectroscopy is commonly used to evaluate the structural quality of the graphene. This technique probes the vibrational modes of molecules and is only applicable to Raman-active specimens, i.e., those whose molecular polarizability changes during vibrational motion following photon excitation.

The Figure I.1 is the Raman spectrum obtained for the undoped graphene powder. The three main peaks correspond to the G, D, and 2D bands. The G-band is associated with carbon-carbon in-plane vibrations, present in all sp2-hybridized carbon structures. The D-band arises from the breathing modes of the carbon rings, primarily occurring at the edges of the graphene lattice, as well as from structural defects originating from hybridization and bond-angle and bond-length disorders. The 2D-band is the most distinctive feature, serving as a fingerprint of graphene, resulting from a two-phonon scattering

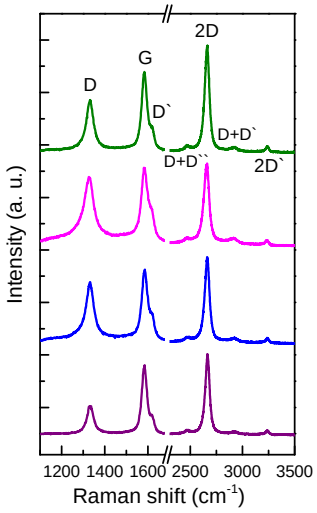

Figure I.1: Raman spectrum of graphene powder.

process. The Full Width at Half Maximum (FWHM) of the 2D-band provides information on the number of monolayers present in each sheet [14]. Furthermore, the relative intensities of these bands are commonly used as indicators of the material's overall quality.

II

Solution Evaporation

Because high-quality free-standing graphene powder is both expensive and difficult to synthesize, the same suspension is reused for approximately three to four depositions in order to minimize material loss. However, repeated use introduces a practical challenge: the constant evaporation of both the electrolyte and the solvent.

To address this issue, the Evaporation Rate (ER) of both solution components was calculated using the third model shown in [56]. This model was selected over the first and second alternatives for the following reasons. The first model incorporates the octanol/air partition coefficient, which applies to systems involving octanol-based solvents and is commonly used for modeling predictions of the partitioning behavior between air and environmental matrices [57]. Since isopropanol is used as the solvent in this work, this model was deemed unsuitable. Both models 2 and 3 were appropriate candidates, but the third model was chosen due to the overestimation of the ER.

Thus, the ER, expressed in $\mu g \cdot m^{-2} \cdot h^{-1}$, was calculated according to the following formula:

$$ER = 1464 \cdot VP \cdot MW \tag{II.1}$$

where VP is the vapor pressure in Pa, and MW is the molecular weight in g/mol. Applying this model revealed that the ER of HCl is approximately 0.772 times that of isopropyl alcohol. Based on this ratio, appropriate corrections were made to the solution volume after each deposition, assuming that the total evaporated volume consisted predominantly of isopropanol.

III

XPS Spectrum Fitting

XPS peak fitting was performed to resolve overlapping signals from chemical bonds with similar binding energies, which exceed the instrumental resolution of the XPS system. The fitting procedure followed a systematic, multi-step approach, as outlined below.

1. Identification of Cu bonds based on Cu 2p3/2 fitting

The first step involved fitting the Cu $2p_{3/2}$ line to distinguish the contributions of copper species on the O 1s line. Although copper itself is not of primary interest in this study, deconvolution of its spectral contribution is necessary to correctly interpret the oxidation-related features within the O 1s line. The relevant copper species within the energy range were CuO, Cu_2O, and $Cu(OH)_2$. During the fitting, either CuO or $Cu(OH)_2$ was found to be present in the spectrum. The fitting model applied was based on the methodology described in [58].

	Line shape	**FWHM constraints (eV)**	**Position constraints (eV)**
Cu	GL(90)	0.90 - 1.66	932.43 - 932.83
Cu_2O	GL(80)	1.15 - 1.50	931.98 - 932.38
$Cu(OH)_2$ 1	GL(30)	2.65 - 3.00	934.47 - 934.87
$Cu(OH)_2$ 2	GL(30)	2.70 - 2.90	939.10 - 939.50
$Cu(OH)_2$ 3	GL(30)	3.56 - 3.76	942.00 - 942.40
$Cu(OH)_2$ 4	GL(30)	1.66 - 1.86	943.92 - 944.32
CuO 1	GL(30)	1.90 - 2.10	933.00 - 933.20
CuO 2	GL(30)	2.90 - 3.10	934.37 - 934.57
CuO 3	GL(30)	0.93 - 1.13	940.41 - 940.61
CuO 4	GL(30)	3.45 - 3.65	941.54 - 941.74
CuO 5	GL(30)	1.07 - 1.27	943.59 - 943.79

Table III.1: Constraints used as a fitting model for the Cu $2p_{3/2}$ line.

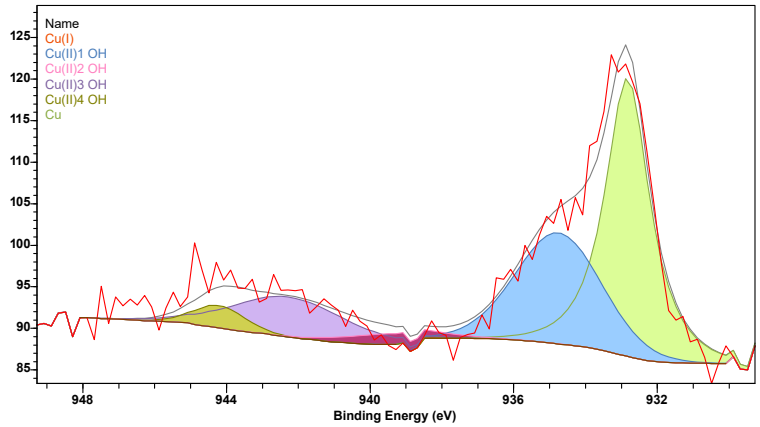

Figure III.1: Example of a fitted Cu $2p_{3/2}$ line.

2. Deconvolution of O 1s bonds

Once the copper oxides were accurately identified, the remaining oxygen bonds were resolved. This step is crucial for quantifying the oxygen species bonded to carbon or nitrogen, which play a key role in characterizing the graphene samples. Because the metallic oxides exist in a different matrix, new sensitivity factors were calculated specifically for graphene. In the C 1s line, C–O bonding configurations such as C–OH and C–O–C cannot be distinguished due to their closely spaced binding energies. The O 1s line, however, provides additional information that helps determine the dominant oxygen functionalities. Contributions from C–O, C=O, and O–C=O were identified and later used as fitting constraints for the C 1s line. Additional features corresponding to adsorbed H_2O and O=C–N were also observed in the O 1s region, with the latter overlapping with $Cu(OH)_2$. Metallic contributions were fitted using the same methodology described in [58], while organic bond assignments followed binding energies in [59].

	Line shape	**FWHM constraints (eV)**	**Position constraints (eV)**
H_2O	GL(30)	1.90 - 2.50	534.00 - 534.80
C-O-C	GL(30)	1.60 - 2.60	532.25 - 532.60
C-OH	GL(30)	1.60 - 2.60	532.55 - 532.90
C=O/O-(C=O*)-C	GL(30)	1.60 - 2.60	531.80 - 532.20
O*-(C=O)-C	GL(30)	1.60 - 2.60	533.20 - 534.60
O=C-N/$Cu(OH)_2$	GL(30)	1.90 - 2.50	531.00 - 531.80
CuO 1	GL(30)	1.30 - 1.50	529.60 - 529.80
CuO 2	GL(30)	1.90 - 2.20	530.80 - 531.10
Cu_2O 1	GL(30)	1.10 - 1.35	530.00 - 530.40
Cu_2O 2	GL(30)	1.10 - 1.35	531.45 - 531.70

Table III.2: Constraints used as a fitting model for the O 1s line.

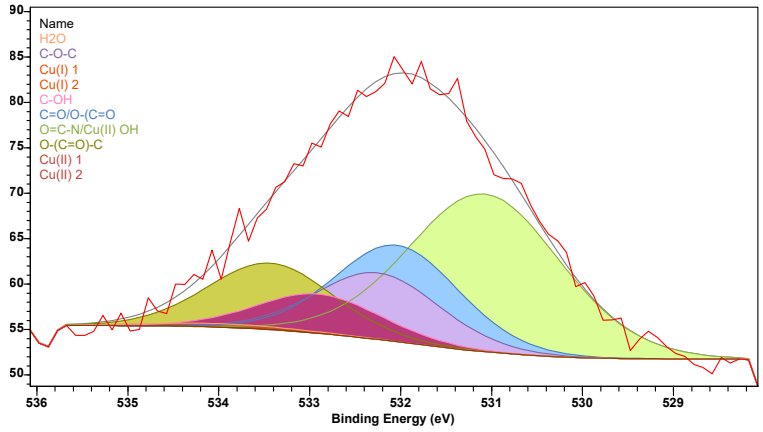

Figure III.2: Example of a fitted O 1s line.

3. Fitting of the N 1s line

The N 1s spectrum was fitted according to the peak model reported in [27], incorporating contributions from pyridinic, pyrrolic, graphitic nitrogen, and nitrogen oxides. As the graphitic nitrogen component is typically minor, the pyrrolic peak provides an indirect means of estimating the number of pentagonal defects within the graphene lattice. This information was later used as an additional constraint during the C 1s fitting.

	Line shape	**FWHM constraints (eV)**	**Position constraints (eV)**
C-(NC)-C	GL(20)	1.4 - 2.0	401.200 - 401.698
C=N-C	GL(20)	1.4 - 2.0	398.051 - 398.800
C-(NH)-C	GL(20)	1.4 - 2.0	399.900 - 400.700
O=N-C	GL(20)	1.4 - 2.0	402.200 - 402.553

Table III.3: Constraints used as a fitting model for the N 1s line.

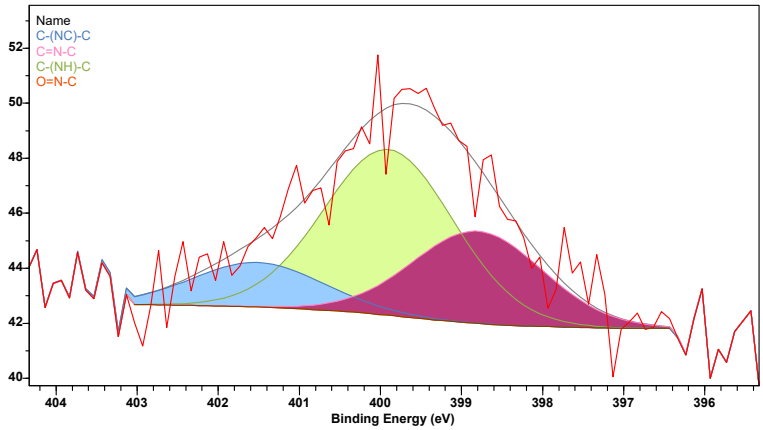

Figure III.3: Example of a fitted N 1s line.

4. Fitting of the C 1s line

The C 1s fitting represented the most complex stage of the procedure. A home-made fitting model, previously developed for graphene and based on [60], was employed as the starting point. The C–O, C=O, and O–C=O peak intensities were constrained to match the quantitative results derived from the O 1s fitting, by adjusting the line shape constraints for C=C. Simultaneously, nitrogen-related contributions were adjusted according to the model in [27], particularly for the C–Clow peak associated with pentagonal structures, by changing its relative area compared to the C=C. Because the C=O peak overlaps with the N–(C_{sp^2}=O) contribution, both were deconvoluted using the ratio obtained from the O 1s fitting, which was then multiplied in the C 1s line.

	Line shape	**FWHM constraints (eV)**	**Position constraints (eV)**
C=C	LA(0.91, 1.88, 10)	0.24 - 1.20	284.3 - 284.8
Satellite	GL(100)	2.50 - 2.70	286.2 - 286.7
π-π*	GL(30)	2.60 - 2.80	291.0 - 291.5
C-C, C-H/C-Chigh/C_{sp^2}-N	GL(30)	0.90 - 1.50	284.8 - 285.3
C-Clow (pentagons)	GL(30)	0.90 - 1.50	283.2 - 284.1
C-O/C_{sp^3}-N/C-N=O	GL(20)	1.40 - 2.40	285.9 - 286.5
C=O/N-(C_{sp^2}=O)/N-C(O)-C	GL(20)	1.40 - 2.40	286.5 - 287.6
C-(O)-O	GL(20)	1.40 - 2.40	288.4 - 288.9

Table III.4: Constraints used as a fitting model for the C 1s line.

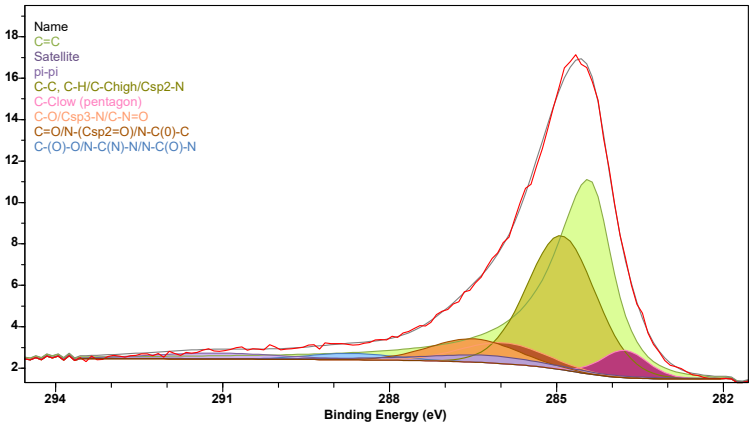

Figure III.4: Example of a fitted C 1s line.

During quantification, special attention was given to bond multiplicity. Certain bonds may contribute disproportionately to the total signal. For instance, the pyrrolic C–(NH)–C structure is counted as half a contribution in the nitrogen line, since the fitting considers

only one N–C bond per nitrogen, despite the presence of two N–C bonds in the actual structure.

The C 1s fitting was ultimately used to determine the sp^2/sp^3 carbon ratio. This involved deconvoluting the C–C, C–H, and C_{sp^2}–N contributions by subtracting twice the nitrogen contribution (to account for the two N–C bonds in pyridinic and pyrrolic nitrogen). The sp^2 fraction was calculated as the sum of the C=C, satellite, and π-π^* plasmon peaks. The final fitting model was systematically applied to all spectra to ensure consistency and comparability across samples.

IV

Supplementary Tables

HCl Content (μL)	TEY	N %	sp^2/sp^3	pyrrolic/pyridinic
20	0.98	2.3	2.19	2.62
40	0.90	2.9	2.13	1.54
60	0.89	3.0	3.07	1.58
80	0.90	2.7	1.95	1.54
100	0.99	1.7	1.79	1.70

Table IV.1: TEY, nitrogen content, sp^2-to-sp^3 ratio, and pyrrolic-to-pyridinic ratio for samples treated with different HCl volumes.

Temperature (°C)	TEY	N %	sp^2/sp^3	pyrrolic/pyridinic
6	0.97	2.6	1.36	3.35
11	0.92	2.4	2.58	1.60
16	0.89	3.0	3.07	1.58
21	0.87			
26	0.95			

Table IV.2: TEY, nitrogen content, sp^2-to-sp^3 ratio, and pyrrolic-to-pyridinic ratio for samples treated with different temperatures.

Voltage (V)	TEY	N %	sp^2/sp^3	pyrrolic/pyridinic
20	1.17	2.2	3.52	0.64
40	0.89	3.0	3.07	1.58
60	0.96	2.8	2.33	1.38
80	0.92	2.4	2.86	1.18

Table IV.3: TEY, nitrogen content, sp^2-to-sp^3 ratio, and pyrrolic-to-pyridinic ratio for samples treated with different voltages.

Sample	V (V)	HCl (μL)	T (°C)	TEY	C %	O %	N %	sp^2/sp^3	pyrrolic/pyridinic
1	40	100	—	1.11	85.8	11.7	—	2.11	—
2	40	100	—	1.23	85.6	13.1	—	3.33	—
3	40	100	—	1.11	87.3	12.7	—	2.11	—
5	40	80	—	1.11	86.7	13.3	—	2.27	—
6	40	150	—	1.22	90.6	9.4	—	1.99	—
7	40	60	—	0.98	96.0	4.0	—	3.72	—
8	40	40	—	1.01	96.1	3.9	—	5.29	—
9	40	130	—	1.14	96.5	3.5	—	2.22	—
15	40	60	16.0	0.90	84.4	12.3	3.2	2.56	1.54
19	40	60	16.0	0.89	90.2	7.2	2.6	3.07	1.58
19 (2)	40	60	16.0	0.89	86.5	7.0	3.4	2.53	1.53
20	60	60	16.0	0.96	86.9	10.3	2.8	2.33	1.38
21	80	60	16.0	0.92	86.9	10.6	2.4	2.86	1.18
22	80	60	—	1.17	72.5	24.5	3.0	—	—
23	20	60	16.0	1.17	90.0	7.8	2.2	3.52	0.64
24	40	80	16.0	0.90	88.9	8.4	2.7	1.95	1.54
25	40	100	16.0	0.99	86.8	11.5	1.7	1.79	1.70
26	40	40	16.0	0.90	89.5	7.6	2.9	2.13	1.54
27	40	20	16.0	0.98	89.2	8.5	2.3	2.19	2.62
28	40	60	11.0	0.92	91.1	6.5	2.4	2.58	1.60
29	40	60	6.0	0.97	84.1	13.3	2.6	1.36	3.35
30	40	60	21.0	0.87	—	—	—	—	—
31	40	60	26.0	0.95	—	—	—	—	—
35	20	40	16.0	0.84	89.0	8.5	2.6	1.70	0.96
36	30	40	18.5	1.16	86.1	11.5	2.4	2.41	1.65
37	40	40	21.0	0.99	84.6	13.2	2.2	2.28	2.39
38	50	40	23.5	0.93	88.8	8.7	2.5	3.13	2.09
39	20	60	18.5	0.83	84.0	13.8	2.2	2.12	1.60
41	30	60	16.0	0.93	88.8	8.9	2.4	2.07	1.47
42	40	60	23.5	0.89	91.6	5.9	2.5	3.07	1.17
43	50	60	21.0	0.84	92.3	5.4	2.3	2.15	1.90
44	20	80	21.0	0.91	89.2	8.2	2.6	2.22	0.98
45	30	80	23.5	0.82	89.1	8.1	2.8	3.20	1.77
46	40	80	16.0	0.85	88.8	8.4	2.8	3.26	1.87
47	50	80	18.5	0.85	90.4	6.4	3.2	2.46	1.80
48	20	100	23.5	0.85	90.9	6.4	2.7	2.75	1.37
49	30	100	21.0	0.90	89.8	6.9	3.3	2.32	1.16
50	40	100	18.5	0.87	90.0	6.9	3.1	2.95	1.51
51	50	100	16.0	0.89	90.0	7.3	2.7	1.93	1.32

Table IV.4: Maximum TEY, atomic quantification and characterization of every sample used in this work.

V

Additional TEY Curve

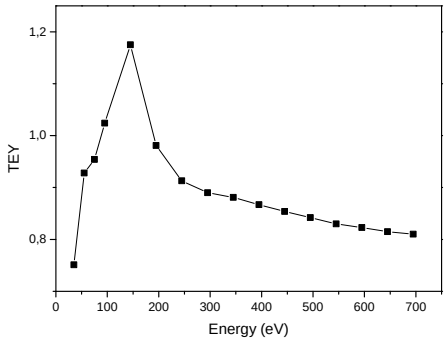

Figure V.1: TEY as a function of the energy of the incident beam.

VI

SEM IMAGES

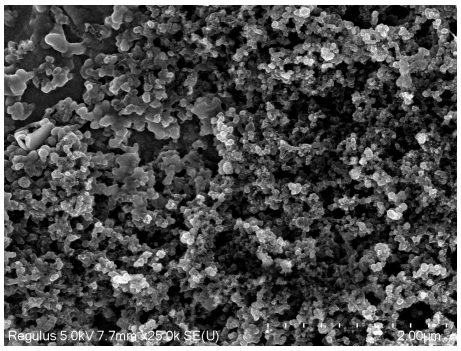

(a) Low HCl concentration.

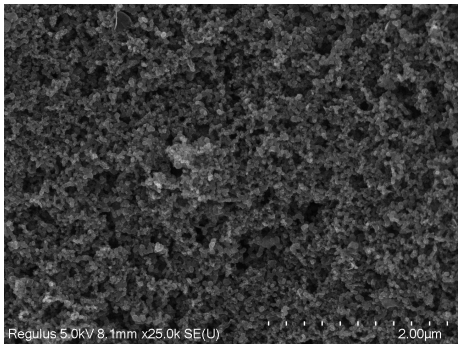

(b) High HCl concentration.

Figure VI.1: SEM image of a sample surface deposited with (a) low HCl concentration and (b) high HCl concentration.

From both SEM images VI.1, it is clear that the HCl concentration affects how the graphene powder is deposited. The nanoparticles are larger, around 75 nm in diameter, when a low HCl concentration is used, while for a higher concentration, the nanoparticles exhibit a diameter of around 25 nm.

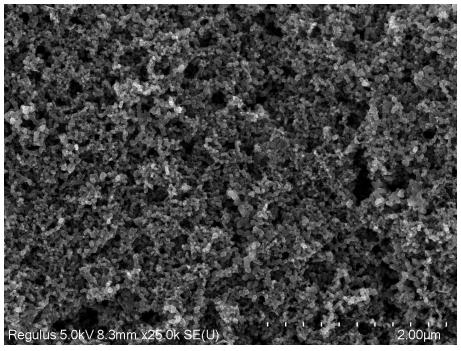

(a) Low applied voltage.

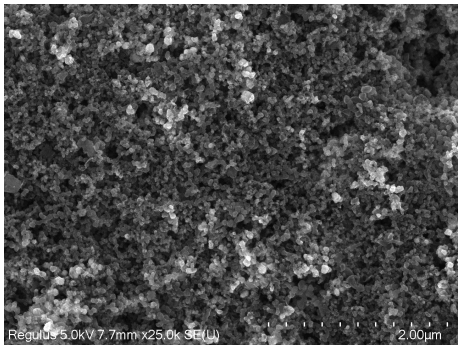

(b) High applied voltage.

Figure VI.2: SEM image of a sample surface deposited with (a) low applied voltage and (b) high applied voltage.

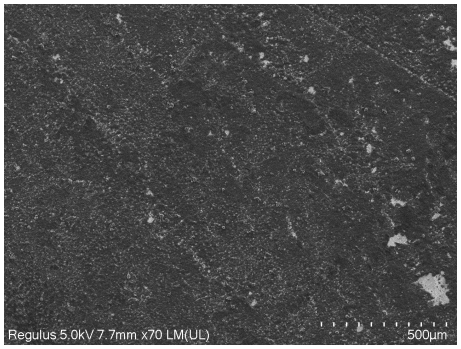

(a) Low applied voltage.

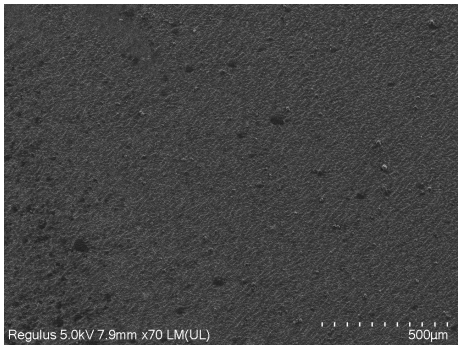

(b) High applied voltage.

Figure VI.3: Low magnitude SEM image of a sample surface deposited with (a) low applied voltage and (b) high applied voltage.

The applied voltage influences how the nanoparticles are distributed along the surface. Lower voltage seems to induce more and deeper holes than high voltage, as can be seen in the Figure VI.2.

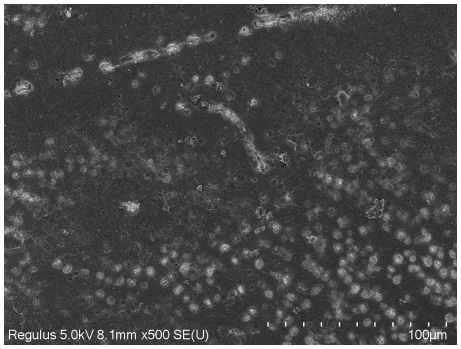

(a) Low temperature control.

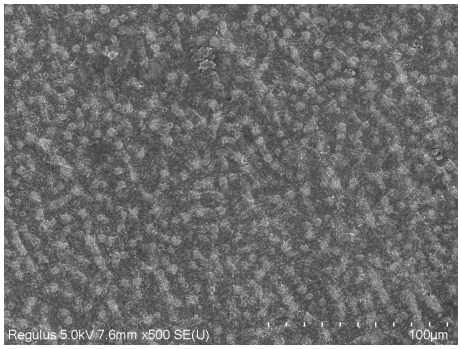

(b) High temperature control.

Figure VI.4: SEM image of a sample surface deposited with (a) low temperature control and (b) high temperature control.

By analysing the SEM images with the same magnitude as Images VI.1 and VI.2, no visual difference can be observed. However, looking at the SEM images VI.4 with lower magnification, the higher is the temperature control, the more stains appear.